Loss of FRIENDLY MITOCHONDRIA (FMT) Restores Chloroplast Proteostasis via Inter-organelle Compensation

Jitae Kim[1*], Changhee Na[2], Pratyush Routray[3], NoA Bae[1], Hanseul Kim[1], Jae-Yeon Kim[1], Da Been Kim[2], Namil Son[4], Zeeshan Nasim[5,6], Ryoung Lee[1], Ji Hyun Kang[2], Geoni Choi[2], Hyoungseok Lee[7], Ji Hoon Ahn[5], Byeong-ha Lee[1], Dong Wook Lee[2,8*], Klaas J. van Wijk[3*]

[1] Department of Life Science, Sogang University, Seoul, 04107, Republic of Korea.

[2] Department of Integrative Food, Bioscience and Biotechnology, Chonnam National University, Gwangju, 61186, Republic of Korea.

[3] Department of Plant Biology, Cornell University, Ithaca, New York 14853, USA.

[4] Department of Plant Sciences, University of Cambridge, Cambridge CB2 3EA, UK.

[5] Department of Life Sciences, Korea University, Seoul 02841, Republic of Korea.

[6] Department of Applied Plant Science, Chonnam National University, Gwangju, 61186, Republic of Korea.

[7] Division of Life Sciences, Korea Polar Research Institute, Incheon, 21990, Republic of Korea.

[8] Department of Bioenergy Science and Technology, Chonnam National University, Gwangju, 61186, Republic of Korea.

* Authors for correspondence: jkim222@sogang.ac.kr (J.K.), ldw4844@jnu.ac.kr (D.W.L.), kv35@cornell.edu (K.J.v.W.)

ABSTRACT

Chloroplast proteostasis is vital for plant development, yet whether cells can actively reprogram organelle communication to restore plastid function when essential protease components fail remains unclear. Using a forward genetic suppressor screen in *Arabidopsis*, we identify loss of the mitochondria-associated protein FRIENDLY MITOCHONDRIA (FMT) as a strong suppressor of the virescent and growth-retarded *clpc1* mutant, which lacks the major chloroplast Clp chaperone ClpC1. Suppression is highly specific and occurs independently of GUN1-mediated retrograde signaling. Integrated multi-omics analyses reveal that *clpc1* and *fmtclpc1* represent two distinct organelle signaling states. In *clpc1*, loss of ClpC1 triggers a plastid stress state characterized by repression of photosynthesis-associated transcription factors, induction of plastid metabolic stress markers, and impaired proteolytic activity. By contrast, loss of FMT shifts the system into a recovery state despite persistent mitochondrial clustering. Mechanistically, FMT negatively regulates *CLPC2*, a ClpC1 paralog, and *fmt*-mediated rescue results from *CLPC2* derepression. Moderately elevated ClpC2 restores *in vivo* proteolysis, as evidenced by recovery of PAA2 substrate turnover, normalization of chloroplast ultrastructure, and reactivation of photosynthesis-related gene expression. Transcriptomic and proteomic profiling further reveal coordinated remodeling of nuclear gene expression and chloroplast protein investment in the recovery state, including reduced cytosolic folding stress and selective induction of jasmonic acid– and salicylic acid–associated signaling networks. Genetic analyses establish that REC1 and REC2 are required for full *CLPC2* induction and phenotypic recovery. Together, our findings uncover a latent inter-organelle compensatory mechanism in which mitochondrial perturbation reprograms nuclear gene expression to restore chloroplast proteostasis when ClpC1 function is compromised.

41 **INTRODUCTION**

42 Plant survival depends on the ability of its energy-producing organelles to communicate and
43 maintain proteostasis despite continual developmental, metabolic, and environmental fluctuations
44 (Gao et al., 2023; Sun and Jarvis, 2023). Chloroplasts and mitochondria rely on thousands of
45 nuclear-encoded proteins that must be precisely synthesized, imported, and folded, rendering both
46 organelles acutely vulnerable to even modest disruptions in protein homeostasis (Sun et al., 2021;
47 Woodson and Chory, 2008). Because failures in these processes compromise photosynthesis,
48 metabolism, and growth, plants must deploy coordinated cellular responses to proteotoxic stress
49 across organelles (Llamas and Pulido, 2022; Lopez et al., 2024; van Wijk, 2024). Although plastid-
50 to-nucleus retrograde signaling pathways that report organelle dysfunction have been extensively
51 characterized, whether cells can transition from a stress-associated transcriptional state to an active
52 recovery configuration that restores chloroplast proteostasis remains largely unknown.

53 In chloroplasts, proteostasis relies heavily on the stromal Clp chaperone–protease system, the most
54 abundant and broadly acting proteolytic machinery in the organelle (Bouchnak and van Wijk, 2021;
55 Rodriguez-Concepcion et al., 2019). The ClpPR core comprises catalytically active ClpP1 and
56 ClpP3–6 and non-enzymatic ClpR1–4 subunits arranged as two stacked heptameric rings (Kim et
57 al., 2013; Kim et al., 2009; Olinares et al., 2011; Sjogren et al., 2006). Substrate unfolding and
58 translocation are mediated by the AAA+ chaperones ClpC1, ClpC2, and ClpD, while accessory
59 proteins such as ClpT1/2, ClpS1, and ClpF contribute to core assembly/stabilization and substrate
60 selection (Kim et al., 2015; Nishimura et al., 2015; Nishimura et al., 2013; Sjogren and Clarke,
61 2011). The turnover of numerous stromal proteins—including the canonical substrate
62 PAA2/HMA8, a copper transporter in the thylakoid—highlights the central role of the Clp
63 machinery in chloroplast protein quality control (Tapken et al., 2015).

64 ClpC1 is a pivotal component of this system. It functions both as the major unfoldase that delivers
65 substrates to the ClpPR core (Rei Liao et al., 2022) and is also involved in quality control of
66 imported proteins at the inner envelope membrane (Paila et al., 2015). Loss of ClpC1 leads to
67 severe chloroplast dysfunction, manifesting as chlorosis, impaired photosynthesis, and markedly
68 reduced growth. Protein-import stress is a known trigger of retrograde transcriptional

69 reprogramming (Richter et al., 2023), and recent work has shown that GUN1 directly binds and
70 stabilizes a subset of plastid RNAs, identifying plastid RNA maturation as a key upstream
71 determinant of plastid-to-nucleus signaling (Tang et al., 2024). These studies define components
72 of the plastid stress response; however, it remains unclear whether plants possess intrinsic
73 mechanisms that can actively reconfigure nuclear gene expression to re-establish chloroplast
74 proteostasis when a core chaperone such as ClpC1 is absent.

75 Mitochondria also undergo dynamic structural and functional remodeling in response to stress
76 (Chustecki et al., 2022; Kacprzak and Van Aken, 2023; Nakamura et al., 2021). The conserved
77 CLU-family protein FRIENDLY MITOCHONDRIA (FMT) maintains mitochondrial distribution,
78 dynamics, and homeostasis; *fmt* mutants exhibit clustered mitochondria, altered organelle contacts,
79 elevated ROS, and growth defects (El Zawily et al., 2014; Logan et al., 2003). FMT associates
80 with cytosolic ribosomes at the mitochondrial surface to promote translation of nuclear-encoded
81 mitochondrial mRNAs (Ayabe et al., 2021; Hemono et al., 2022), and contributes to mitophagy
82 during de-etiolation (Ma et al., 2021). Despite these well-characterized mitochondrial functions,
83 whether mitochondrial perturbation can influence plastid proteostasis or alter nuclear
84 transcriptional states linked to chloroplast function has not been explored. Arabidopsis encodes
85 three FMT-related homologues—*REC1-REC3*—that regulate chloroplast compartment size, and
86 in tomato they additionally influence plastid development and plastid-related gene expression (Hu
87 et al., 2024; Larkin et al., 2016), although their functions in organelle stress responses remain
88 unresolved.

89 To identify pathways capable of actively restoring chloroplast proteostasis when ClpC1 function
90 is lost, we performed a forward EMS suppressor screen in the severe chlorotic *clpc1-1* mutant.
91 Multiple independent suppressors carried mutations in *FMT*, revealing an unexpected connection
92 between mitochondrial perturbation and recovery of chloroplast function. RNA-seq and
93 comparative proteomics uncovered coordinated remodeling of nuclear gene expression and
94 chloroplast protein investment, consistent with a transition from a plastid stress state to a recovery
95 state. We show that loss of *FMT* is associated with increased *REC2* expression and transcriptional
96 upregulation of *CLPC2,* a ClpC1 paralog, and that *REC1* and *REC2* are required for full *fmt*-
97 mediated compensation. Elevated ClpC2 functionally substitutes for ClpC1, restoring chloroplast

98 proteostasis, pigmentation, and growth. Together, these findings reveal an inter-organelle
99 compensatory mechanism in which mitochondrial perturbation enables reprogramming of nuclear
100 gene expression to re-establish chloroplast proteostasis when ClpC1 function is compromised.

101

102 **RESULTS**

103 **Suppressor Screen Identifies Green Leaf Mutants in the *clpc1-1* Background**

104 To identify new genetic factors involved in chloroplast proteostasis and to gain insight into cellular
105 responses to *CLPC1* deficiency, we performed a forward genetic suppressor screen in the *clpc1-1*
106 background. The *clpc1-1* mutant exhibits a pronounced virescent and growth-retarded phenotype,
107 enabling efficient visual identification of M2 individuals with restored greening and enhanced
108 growth. Approximately 10,000 *clpc1-1* seeds were mutagenized with ethyl methanesulfonate
109 (EMS), and the resulting M2 progeny were screened for recovery of the chlorotic phenotype. We
110 identified ~10 independent suppressor candidates showing partial or near-complete restoration of
111 the wild-type phenotype. Among these, four lines with the strongest recovery—approaching wild
112 type—were selected for detailed characterization (Figure 1A, B). The remaining candidates
113 displayed weaker phenotypes and were not pursued further in this study.

114 To genetically map the causal suppressor mutations, each of the four selected lines—designated
115 *socc* (suppressor of *clpc1*)—was backcrossed to the parental *clpc1-1* mutant. In the segregating
116 BC1F2 populations, the green-leaf phenotype appeared at an approximate 1:3 ratio
117 (green:chlorotic), consistent with suppression conferred by a single recessive locus. For each *socc*
118 line, genomic DNA was extracted from more than 50 BC1F2 individuals displaying either green
119 or chlorotic phenotypes. DNA from plants of the same phenotype was pooled and subjected to
120 whole-genome sequencing. Candidate causal variants were then identified by comparing allele
121 frequency differences between the green and chlorotic bulks using the SIMPLE pipeline
122 (Wachsman et al., 2017) (Figure 1A).

Whole-Genome Sequencing Reveals Recurrent Mutations in *FMT*

Analysis of single nucleotide polymorphism (SNP) frequencies across bulked segregant pools revealed that all four independent suppressor lines carried distinct EMS-induced mutations in a common gene, *FMT* (*At3g52140*). Representative phenotypes of these lines are shown in Figure 1B, each exhibiting substantial restoration of greening relative to the *clpc1-1* parental mutant.

In *socc43-1 clpc1-1*, a missense mutation in exon 10 of *FMT* results in a Glu534Lys substitution. In contrast, *socc20-1*, *socc20-4*, and *socc39-1* carry mutations affecting canonical splice donor or splice acceptor sites, or adjacent splice regions, all predicted to disrupt proper splicing and impair *FMT* function. Notably, *socc43-1* also harbors a synonymous substitution near an exon–intron boundary that may affect splicing efficiency (Figure 1C; Supplemental Table 1). The independent recovery of distinct EMS-induced mutations in *FMT* across multiple suppressor lines strongly implicates *FMT* as the candidate locus underlying suppression of *clpc1-1*.

Complementation Confirms *FMT* as the Causal Suppressor Gene

To test whether loss of *FMT* is responsible for suppression, each of the four EMS-derived suppressor lines was transformed with a wild-type *FMT* genomic construct driven by its native promoter (*pFMT::FMT*). In all cases, reintroduction of functional *FMT* restored the chlorotic and stunted phenotype of *clpc1-1*, thereby reversing suppression (Figure 1D). These complementation results provide strong functional evidence that disruption of *FMT* is directly responsible for the green, growth-recovered phenotype of the suppressor lines.

T-DNA Insertion Mutants Validate *FMT* as the Causal Suppressor Gene

To further validate *FMT* as the gene responsible for suppression of the *clpc1-1* phenotype, we analyzed two independent T-DNA insertion alleles, *fmt-3* and *fmt-4*. When combined with *clpc1-1*, both double mutants (*fmt-3clpc1-1* and *fmt-4clpc1-1*) exhibited restored greening and growth, phenocopying the EMS-derived suppressor lines (Figure 1E).

147 To assess the effects of EMS- and T-DNA–induced mutations on *FMT* transcript accumulation,
148 we performed semi-quantitative RT-PCR using four primer sets spanning different regions of the
149 *FMT* coding sequence (1F1R–4F4R) (Supplemental Figure 1A, B). In *fmt-3*, *FMT* transcript levels
150 were strongly reduced across all primer sets, consistent with a severe knockdown. In contrast, *fmt-*
151 *4* showed loss of amplification at the C-terminal region (3F3R and 4F4R), consistent with a null
152 allele. EMS-derived *socc* alleles exhibited aberrant splicing patterns, with *socc20-1*, *socc20-4*, and
153 *socc43-1* producing additional higher-molecular-weight bands with the 3F3R primer set,
154 indicative of mis-spliced transcripts. Across all EMS alleles tested, overall *FMT* transcript
155 abundance was reduced relative to *clpc1-1* (Supplemental Figure 1B), consistent with partial loss
156 of function.

157 As expected, *CLPC1* transcripts were absent in all *clpc1-1* backgrounds, confirming that *clpc1-1*
158 is a null allele and that suppression does not arise from *CLPC1* reactivation. Notably, *FMT*
159 transcripts were elevated in *clpc1-1* relative to wild type, suggesting transcriptional upregulation
160 of *FMT* in response to chloroplast dysfunction caused by *CLPC1* loss. Together, these data validate
161 the molecular identity of both T-DNA and EMS-derived suppressor alleles and demonstrate that
162 suppression arises through loss of *FMT* function rather than restoration of *CLPC1*.

163 To test whether *fmt*-mediated suppression restores chloroplast performance, we measured
164 maximum quantum efficiency of PSII (Fv/Fm) and total pigment content. Both *fmt-3clpc1-1* and
165 *socc20-1clpc1-1* displayed significantly higher Fv/Fm values than *clpc1-1*, approaching wild-type
166 levels (Figure 1F, left). Total chlorophyll and carotenoid contents showed a similar trend (Figure
167 1F, middle and right). These results indicate that *fmt*-mediated suppression improves chloroplast
168 function—enhancing photosynthetic efficiency and pigment accumulation in the *clpc1-1*
169 background.

170 **Heteroallelic Crosses Confirm *FMT* as the Causal Suppressor Gene**

171 To confirm that the EMS-derived *socc* suppressor mutations disrupt *FMT* rather than other loci,
172 we performed heteroallelic complementation tests. F1 progeny from *fmt-3clpc1-1*×*fmt-4clpc1-1*
173 crosses exhibited the same suppressed phenotype as the parental lines, confirming allelism

174 between the two T-DNA insertions (Supplemental Figure 2A). Likewise, F1 progeny from each
175 EMS-derived *socc_clpc1-1×fmt-3clpc1-1* cross displayed the suppressed phenotype, indicating
176 failure to complement. These results establish that all four *socc* alleles represent independent loss-
177 of-function mutations in *FMT*.

178 **CRISPR-Derived *clpc1* Null Alleles Confirm Allele-Independent Suppression by *fmt***

179 To rule out T-DNA–specific epigenetic suppression of *clpc1-1*, we generated two independent
180 CRISPR-derived null alleles (*clpc1-4*, *clpc1-5*), each carrying frameshift mutations in exon 4. Both
181 alleles phenocopied *clpc1-1* and failed to complement it in heteroallelic crosses (Supplemental
182 Figure 2B). Importantly, both were robustly suppressed by *fmt-3* (Figure 1G), demonstrating that
183 *fmt*-mediated rescue is allele-independent and does not result from epigenetic reactivation (Gao
184 and Zhao, 2013; Jia et al., 2015) of the T-DNA insertion. Together, these results establish *FMT*
185 loss of function as the causal basis of all recovered EMS suppressors and demonstrate that
186 disruption of *FMT* restores chloroplast performance in multiple *clpc1* null alleles through a
187 genuine genetic interaction with *CLPC1*.

188 ***fmt* Specifically Suppresses *clpc1-1* but Not Other Chloroplast Proteostasis or Import**
189 **Mutants**

190 We next investigated whether *fmt*-mediated suppression is specific to *CLPC1* or extends to other
191 components of chloroplast proteostasis and protein import. To test this, we examined genetic
192 interactions between *fmt* and representative mutants affecting distinct subunits of the Clp protease
193 complex and the chloroplast import machinery.

194 To determine whether suppression extended to other components of the Clp chaperone-protease
195 complex, we crossed *fmt* with *clpr2-1* (Rudella et al., 2006), a non-catalytic core subunit mutant,
196 and with the *clpt1-2clpt2-1* double mutant (Kim *et al.*, 2015), which lacks accessory proteins
197 critical for Clp complex stability and assembly. Neither *fmt-3* nor *fmt-4* suppressed the pale, small
198 phenotype of *clpr2-1* (Figure 2A), and *fmt-4* did not rescue the severe developmental defects of

199 *clpt1-2clpt2-1* (Figure 2B). These results indicate that *fmt* suppression is not broadly applicable to
200 defects in the Clp protease complex and may act specifically at the level of ClpC1.

201 We next tested genetic interactions between *fmt* and mutants defective in the chloroplast protein
202 import. The *ppi1-1* mutant, lacking the TOC33 receptor and displaying a pale-green, small size
203 seedling phenotype (Kubis et al., 2003), was crossed with *fmt-3*. Similarly, the small and pale
204 *tic40-4* mutant, defective in a co-chaperone of the TIC complex (Bedard et al., 2017), was crossed
205 with both *fmt-3* and *fmt-4*. In all cases, the resulting double mutants displayed exacerbated
206 phenotypes relative to the respective single mutants. Specifically, *fmt-3ppi1-1* plants were smaller
207 than *ppi1-1* alone, and *fmt-3tic40-4* and *fmt-4tic40-4* plants were markedly smaller and more
208 chlorotic than *tic40-4* (Figure 2C, D). These results show that *fmt* does not restore defects in
209 chloroplast protein import and that loss of *FMT* further impairs plastid function when import is
210 compromised. Thus, *fmt*-mediated suppression is highly specific to *clpc1-1* and does not reflect
211 general rescue of Clp or import defects.

212 ***fmt*-mediated suppression of *clpc1-1* operates independently of GUN1**

213 To examine whether *fmt* interacts with plastid-to-nucleus retrograde signaling pathways (Richter
214 *et al.*, 2023), we combined *fmt* alleles with *gun1-101*. While *fmt* and *gun1-101* single mutants were
215 uniformly green, all *fmtgun1-101* double mutants displayed a distinctive variegated phenotype (Fig.
216 2E), indicating that loss of *GUN1* results in unstable chloroplast biogenesis and function in *fmt*
217 backgrounds.

218 We next tested whether *GUN1* is required for *fmt*-mediated suppression of *clpc1-1*. The *clpc1-*
219 *1gun1-101* double mutant exhibited a more severe phenotype than *clpc1-1* alone (Figure 2F).
220 However, introduction of *fmt-3*, *fmt-4*, or *socc20-1* into the *clpc1-1gun1-101* background restored
221 greening and growth (Figure 2F), demonstrating that suppression occurs in the absence of *GUN1*.
222 Notably, the triple mutants retained the variegation characteristic of *fmt gun1-101*, suggesting that
223 loss of ClpC1 and loss of GUN1 have different underlying molecular causes (Figure 2F).

224 ***fmt* Suppressor Lines Restore Chloroplast Ultrastructure in *clpc1-1* Despite Persistent**
225 **Mitochondrial Clustering**

226 Previous studies showed that wild-type chloroplasts exhibit compact morphology with well-
227 stacked thylakoids, whereas *fmt* mutants retain normal chloroplast ultrastructure but display
228 abnormal mitochondrial clustering and aggregation (El Zawily *et al.*, 2014). Consistent with its
229 severe chlorotic phenotype, *clpc1-1* chloroplasts appeared swollen and irregular, with reduced
230 stromal density and poorly organized thylakoid membranes (Figure 3A). In contrast, *fmt-3clpc1-1*
231 double mutants exhibited compact chloroplasts with dense stroma and well-developed grana stacks,
232 closely resembling wild type (Figure 3A). Mitochondria in the double mutants remained tightly
233 clustered, reflecting the characteristic *fmt* phenotype.

234 ***fmt* Suppressor Lines Normalize ClpC1-Dependent Substrate Selector and Substrate Levels**

235 To assess whether *fmt*-mediated suppression restores chloroplast proteostasis, we examined
236 steady-state levels of ClpC1-associated proteins by immunoblotting (Figure 3B). ClpF (an N-
237 recognin adaptor), ClpS1 (a substrate selector), and PAA2 (a thylakoid Cu-transporting ATPase
238 and Clp substrate) were analyzed as representative markers of ClpC1-dependent function. PAA2
239 degradation requires ClpC1 under copper-replete conditions (Tapken *et al.*, 2015), making it a
240 sensitive marker of ClpC1-dependent activity. Immunoblotting showed that *clpc1-1* accumulated
241 high levels of ClpF, ClpS1, and the ClpC1 substrate PAA2 (Fig. 3B), consistent with previous
242 reports (Nishimura *et al.*, 2015; Nishimura *et al.*, 2013; Tapken *et al.*, 2015). In *fmt-4clpc1-1* and
243 *socc20-1clpc1-1*, ClpS1 and PAA2 levels decreased toward wild-type abundance, and ClpF levels
244 trended downward.

245 ***fmt* Suppressor Lines Restore Clp Protease Activity**

246 To directly assess whether suppression restores functional proteolysis, we performed a PAA2
247 degradation assay under $CuSO_4$-replete conditions, following the approach of (Tapken *et al.*, 2015).
248 PAA2 (HMA8) is a thylakoid Cu-transporting ATPase that is selectively degraded under high Cu^{2+}

249 conditions in a ClpC1-dependent manner. Arabidopsis seedlings were grown on MS agar plates
250 with or without $CuSO_4$, and PAA2 abundance was analyzed from total protein extracts (Figure
251 3C). In wild-type, $CuSO_4$ treatment caused a pronounced decrease in PAA2 levels, consistent with
252 active Clp-mediated degradation. In *clpc1-1*, PAA2 remained highly abundant and insensitive to
253 $CuSO_4$, indicating a strong defect in proteolytic turnover. Strikingly, Cu^{2+}-dependent PAA2
254 degradation was restored in all three *fmt*-mediated suppressor lines: *fmt-3clpc1-1*, *fmt-4clpc1-1*,
255 and *socc20-1clpc1-1*. In each case, $CuSO_4$ treatment led to a marked reduction in PAA2 levels,
256 closely resembling the wild-type response and demonstrating that *fmt* suppression restores Cu^{2+}-
257 dependent Clp protease activity. In contrast, *fmt-3clpr2-1* exhibited persistent PAA2 accumulation
258 similar to *clpr2-1*, reinforcing that *fmt* selectively suppresses *clpc1-1* but does not bypass defects
259 in the Clp protease core.

260 **_fmt_-Mediated Suppression of _clpc1-1_ Involves Transcriptional Upregulation of _CLPC2_**

261 The recovery of chloroplast structure and proteostasis in *fmtclpc1-1* mutants (Figure 3A, C)
262 suggested that *fmt* may activate a compensatory mechanism that restores Clp chaperone capacity
263 in the absence of ClpC1. Because ClpC1 and ClpC2 have partially overlapping functions—with
264 ClpC2 able to substitute for ClpC1 when expressed at higher levels—we asked whether *fmt*
265 suppressors increase *CLPC2* expression.

266 To test this, we quantified *CLPC2* transcript abundance, along with *CLPD* as a related control, by
267 RT–qPCR across multiple genotypes (Figure 3D). *CLPC2* expression was approximately twofold
268 higher in *fmt-3*, *fmt-4*, *fmt-3clpc1-1*, *fmt-4clpc1-1*, and *socc20-1clpc1-1* relative to wild type and
269 *clpc1-1*, indicating that loss of *FMT* consistently induces *CLPC2* transcription. In contrast, *CLPD*
270 transcript levels showed only minor variation among genotypes and did not exhibit the coordinated
271 upregulation seen for *CLPC2*, indicating that the compensatory response is specific to *CLPC2*
272 rather than a general induction of Clp chaperone genes.

273 **Native Promoter–Driven Elevation of _CLPC2_ Is Sufficient to Rescue the _clpc1-1_ Phenotype**

274 Because *CLPC1* expression is normally far higher than *CLPC2* in wild-type plants, we next asked
275 whether the moderate increase in *CLPC2* observed in *fmtclpc1-1* suppressor lines is sufficient to
276 account for phenotypic rescue. To test this, and to avoid artifacts associated with strong
277 constitutive promoters, we generated *pCLPC2::genomic-CLPC2/clpc1-1* lines expressing
278 genomic *CLPC2* under its native promoter.

279 These lines showed 2-4-fold increases in *CLPC2* transcripts compared with *clpc1-1* and showed
280 proportional restoration of greening and pigment accumulation (Fig. 3E–G) (*i.e.* higher *CLPC2*
281 transcript levels result in better suppression/complementation), demonstrating that a several-fold
282 increase in ClpC2 is enough to offset complete loss of *clpc1-1*. The scaling of *CLPC2* expression
283 across the overexpression lines is consistent with differences in *gCLPC2* copy number, and
284 indicates that the promoter is not saturated in the *clpc1-1* background.

285 Together, these findings indicate that physiologically modest upregulation of *CLPC2* is sufficient
286 to compensate for loss of *CLPC1* function. This finding complements earlier work by (Kovacheva
287 et al., 2007), who showed that strong *35S::CLPC2* overexpression can also rescue *clpc1* defects,
288 although high expression occasionally triggered co-suppression-associated albino phenotypes.

289 ***FMT* Expression Level Negatively Correlates with Growth and Chlorosis Severity in *clpc1-***
290 ***1***

291 To further examine how *FMT* expression levels influence the *clpc1-1* phenotype, we generated
292 *pFMT::FMT/clpc1-1* lines in which *FMT* was expressed at elevated levels under its native
293 promoter, minimizing non-physiological expression patterns sometimes associated with the 35S
294 promoter. Seven independent OE lines were obtained, spanning a broad range of rosette size and
295 chlorosis severity (Supplemental Figure 3A). Notably, higher *FMT* expression consistently
296 correlated with smaller rosettes and reduced greening. Lines with the strongest overexpression
297 (e.g., OE#1) displayed the most pronounced chlorosis, whereas lines with lower expression (e.g.,
298 OE#7) more closely resembled *clpc1-1*. Semi-quantitative RT-PCR confirmed graded differences
299 in *FMT* transcript abundance among these lines (Supplemental Figure 3B), and densitometric

300 analysis revealed a clear inverse relationship between *FMT* transcript level and phenotype severity
301 (Supplemental Figure 3C).

302 Based on this expression gradient, we selected OE#1 and OE#2—the two lines with the highest
303 *FMT* transcript accumulation—for detailed physiological and molecular characterization (Figure
304 3H–I).

305 **Overexpression of *FMT* Represses *CLPC2* and Exacerbates the *clpc1-1* Phenotype**

306 We noticed that the smaller, chlorotic rosette phenotype of *pFMT::FMT/clpc1-1* overexpression
307 lines (OE#1 and OE#2) closely resembled that of the *clpc1-1clpc2-2* double mutant (Figure 3H).
308 *clpc2-2* is a partial loss-of-function allele, and *clpc1-1clpc2-2* plants exhibit a smaller, more
309 chlorotic phenotype than *clpc1-1*, whereas the *clpc2-3* null mutant causes embryo lethality in the
310 *clpc1-1* background (Nishimura *et al.*, 2013). Although the two *FMT* overexpression lines were
311 slightly larger than *clpc1-1clpc2-2*, they were markedly smaller and paler than *clpc1-1*, suggesting
312 that elevated *FMT* expression exacerbates the *clpc1-1* phenotype by repressing—rather than
313 supporting—*CLPC2*.

314 To verify the molecular basis of this phenotype, we quantified *CLPC2* transcript levels by RT-
315 qPCR (Figure 3D). *CLPC2* transcript abundance in the *pFMT::FMT/clpc1-1* overexpression lines
316 was approximately 60-70% of *clpc1-1* levels, while the *clpc1-1clpc2-2* double mutant retained
317 about 50% of *clpc1-1* expression (Figure 3D). The lower *CLPC2* expression in *clpc1-1clpc2-2* was
318 consistent with its more severe phenotype (Figure 3H). These results demonstrate that *FMT*
319 overexpression represses *CLPC2* transcription in the *clpc1-1* background, supporting the
320 conclusion that *FMT* functions as a negative regulator of *CLPC2*.

321 To determine whether these transcriptional differences impact chloroplast performance, we
322 measured the maximum quantum yield of PSII (Fv/Fm) and pigment content (Figure 3I). Both
323 *FMT* OE lines and *clpc1-1clpc2-2* exhibited significantly reduced Fv/Fm and pigment levels
324 relative to *clpc1-1*, consistent with their more chlorotic and stunted phenotypes.

325 Together, these findings indicate that *fmt*-mediated suppression of *clpc1-1* involves transcriptional
326 upregulation of *CLPC2*, which compensates for loss of ClpC1. Conversely, elevated *FMT*
327 expression reduces *CLPC2* transcript abundance and phenocopies partial *CLPC2* deficiency,
328 exacerbating the *clpc1-1* phenotype.

329 **RNA-seq reveals coordinated transcriptional remodeling associated with *clpc1* suppression**

330 To better understand the molecular phenotypes of *fmt* and *clpc1-1,* and suppression of the *clpc1-1*
331 phenotype in *fmtclpc1-1*, we performed RNA-seq analysis of Arabidopsis seedlings at
332 developmental stage 1.07 for WT, *fmt-3, clpc1-1*, *fmt-3clpc1-1* and *FMT/clpc1-1* (OE#1). After
333 mapping, quality control, and normalization, mRNA expression values were obtained for 21,202
334 genes (Supplemental Data Set 1A), and pairwise differential expression statistics were calculated
335 for downstream analyses. Principal Component Analysis (PCA) showed a very distinct signature
336 for *clpc1,* which was further enhanced in *FMT*/*clpc1* (Fig. 4A). *fmtclpc1* was more closely related
337 to WT, whereas *fmt* was very similar to WT but remained distinct from *fmtclpc1*. The PCA results
338 are consistent with the observed phenotypes across these five genotypes.

339 We extracted all genes that showed a pairwise difference of at least 2-fold (x<0.5 or x>2) with
340 P<0.01 in at least one of the 10 possible comparisons across genotypes (Supplemental Data Set
341 1B). This resulted in 4,745 nuclear protein-coding genes that we annotated for subcellular protein
342 location and function (Supplemental Data Set 1B). Gene cluster analysis showed three main
343 clusters (I, II, III) that each further separated into three subclusters (Fig. 4B). Cluster I is dominated
344 by genes for which the mRNA is enriched in *clpc1* and *FM*T/*clpc1* often with most enhanced
345 expression in *FMT/clpc1*. Cluster II is enriched for genes that are reduced in *clpc1* and *FMT/clpc1.*
346 Cluster III contains genes with mRNA generally enriched only in *fmtclpc1* as compared to the
347 other four genotypes. MapMan (Thimm et al., 2004) functional bin analysis shows that cluster I
348 and III are both highly depleted for genes encoding photosynthetic proteins (Fig. 4C). Cluster I,
349 but not clusters II and III, is also relatively low in genes involved in mitochondrial electron
350 transport/ATP synthesis (bin 9), tetrapyrrole metabolism (bin 19) and amino acid metabolism (bin
351 13). Cluster I is most enriched for genes involved in DNA and RNA related processes. Most genes
352 in cluster III (subcluster 8 and 9) are expressed much higher in *fmtclpc1* than in any of the other

353 four genotypes; this cluster is especially enriched for signaling (bin 30) and stress (bin 20) (Fig.
354 4C). Figure 4D shows the bin-cluster analysis for the genes encoding experimentally confirmed
355 plastid-, mitochondrial-, and dually localized proteins (556, 58 and 15 genes, respectively). 72%
356 belong to cluster II. RNA metabolism shows strong enrichment for cluster I – many of these are
357 PPR proteins with functions in editing and RNA processing of plastid- or mitochondria-encoded
358 genes. Proteins involved in the protein life cycle (bin 29) are also enriched in this cluster I.
359 Photosynthetic functions (bin 1) and starch metabolism (bin 2) are nearly exclusively in cluster II,
360 consistent with the loss of photosynthesis phenotypes of *clpc1* and *FMT/clpc1*. In contrast, amino
361 acid metabolism (bin 13), sulfur assimilation (bin 14), and hormone synthesis (bin 17 - nearly
362 exclusively proteins involved in plastid jasmonate metabolism, including allene oxide cyclase 1,
363 2, 3, and 4; allene oxide synthase; and lipoxygenase 1 and 2) are enriched in cluster III.

364 Subcluster 4 (376 genes) stands out for its high mRNA levels in the *fmt* line compared to the other
365 four genotypes. Many of the genes with the most pronounced expression profiles encode
366 mitochondrial proteins (Supplemental Figure 4A), including alternative oxidase 1A (AOX1A),
367 stomatin-like protein 2 (SLP2), heat shock protein HSP23.5, DUF295 domain protein DOB5, and
368 external NAD(P)H dehydrogenase subunit B3 (NDH-B3), all of which are reported to have low
369 basal expression levels (Elhafez et al., 2006). AOX1A and NDH-B3 partially uncouple respiration
370 from mitochondrial ATP production and thereby reduce mitochondrial reactive oxygen species
371 (ROS) production (Selinski et al., 2018). AOX1A is a marker of the mitochondrial retrograde
372 response (Wang et al., 2020). SLP2 affects protein abundance and activity of respiratory complex
373 I, likely through effects on its assembly and/or stability (Gehl et al., 2014; Gehl and Sweetlove,
374 2014). HSP23.5 is a member of the HSP20-like chaperone superfamily; although this specific
375 protein has not been characterized, mitochondrial HSP20 chaperones are important for facilitating
376 protein folding within mitochondria, particularly under stress conditions (Waters and Vierling,
377 2020). DUF295 domain protein DOB5 has not been characterized but is part of the large DUF295
378 family (Lama et al., 2019). Notably, subcluster 4 contains eight DUF295 family members, seven
379 of which are predicted to encode mitochondrial proteins. Many mitochondrial DUF295 proteins
380 are induced by mitochondrial dysfunction (Lama *et al.*, 2019), which is highly consistent with their
381 elevated abundance in the *fmt* background.

382 Subclusters eight and nine (within cluster III) contain genes with high mRNA levels in *fmtclpc1*
383 compared to the other four genotypes. These genes may provide clues about the nature of *clpc1*
384 suppression by *fmt.* Among the confirmed plastid and mitochondrial proteins, we identified five
385 genes for which the RNA levels in *fmtclpc1* were more than threefold higher than in each of the
386 other four genotypes (Supplemental Figure 4B). Surprisingly, all five are involved in jasmonate or
387 salicylic acid metabolism or response; these include two allene oxide cyclases (AOC1 and AOC3)
388 and lipoxygenase 3 involved in JA synthesis (Bittner et al., 2022), the plastid envelope MATE
389 transporter EDS5, which is likely involved in SA export from plastids (Rekhter et al., 2019), and
390 mitochondrial arginase 2 (ARGAH2), which is highly induced by methyl jasmonate (Brownfield
391 et al., 2008). Furthermore, the plastid Sigma1 interacting factor (Sib1, At3g56710) (Morikawa et
392 al., 2002) is also highly expressed in *fmtclpc1* compared to *clpc1* (6.3-fold) and 2-3 fold compared
393 to WT and *fmt*. Sib1 has been shown to be involved in JA and SA responses either within the
394 chloroplast or in the nucleus (Xie et al., 2010; Zhang et al., 2022). Overexpression of Sib1 causes
395 hyperactivation of defense-related genes following SA and JA treatments (Xie *et al.*, 2010). These
396 results suggest that JA and SA play an important role in the suppression of *clpc1* by *fmt.*

397 Some 30 transcription factors (TFs) have been highlighted as important during chloroplast and/or
398 mitochondrial dysfunction, stress, retrograde signaling, or plastid biogenesis and proteostasis
399 (Bittner *et al.*, 2022; He et al., 2023; Hernandez-Verdeja, 2025; Wang et al., 2018; Wang *et al.*,
400 2020) (Supplemental Table 3). Fifteen of these TFs showed at least one pairwise differential
401 expression (adj. P<0.01) (Supplemental Data Set 1B; Fig. 4B). Four of these—HSFA2, GLK1,
402 BBX15, and WRKY40 (At2g26150, At2g20570, At1g25440 and At1g80840)—showed
403 significant differential expression patterns consistent with contributing to *clpc1* suppression (Fig.
404 4E). HSFA2 (cluster II-4) was strongly upregulated in *fmt* compared to WT but reduced in *clpc1,*
405 with partial restoration in *fmtclpc1.* Notably, HSFA2 was also elevated in the *FMT/clpc1*
406 background despite a more chlorotic and smaller phenotype, indicating that HSFA2 induction does
407 not correlate with phenotypic recovery and is unlikely to be a primary driver of *clpc1* suppression.
408 In contrast, GLK1 (cluster II-6) was unaffected in *fmt* but strongly suppressed in *clpc1* and
409 *FMT/clpc1,* with partial restoration in *fmtclpc1.* The zinc-finger TF BBX15 (cluster II-4) (Ohmiya
410 et al., 2019) was upregulated in *fmt* and downregulated in *clpc1* and *FMT/clpc1,* but restored to
411 WT levels in *fmtclpc1*. WRKY40 (cluster III-9), which is involved in attenuation of basal pathogen

412 defense and is upregulated by GLK1/2 (Lee et al., 2023), was elevated in *fmtclpc1,* likely reflecting
413 a genetic interaction between *fmt* and *clpc1*. We note that the RNA levels of the well-studied TFs
414 HY5 and GLK2 (both positive regulators of genes encoding chloroplast proteins involved in
415 photosynthesis and chlorophyll synthesis), as well as the direct GLK1 target BBX14 (a homolog
416 of BBX15) implicated in chloroplast development (Atanasov et al., 2024), were not significantly
417 different (adj. P<0.01) across these five genotypes.

418 **Comparative proteomics reveals coordinated remodeling of chloroplast protein investment**
419 **during *clpc1* suppression**

420 To understand the suppression effect of *fmt* on the *clpc1* leaf proteome phenotype, total leaf
421 proteomes of *clpc1-1* and *fmt-3clpc1-1* were compared by quantitative proteomics. A total of 2,975
422 proteins and protein groups comprising close homologs were identified, most of which (95%) were
423 detected in both genotypes (Supplemental Data Set 2). Correlation analysis and principal
424 component analysis (PCA) showed clear separation between genotypes and low variation among
425 biological replicates (Supplemental Figure 5A,B). Of the identified proteins, 1,266 (43%) were
426 localized to chloroplasts and/or mitochondria, representing ~65% of all matched spectra. The five
427 thylakoid complexes involved in the light reactions (PSII, PSI, cytochrome b6f, NDH and ATP
428 synthase) all increased between 32% and 49%, whereas the Calvin-Benson cycle enzymes
429 collectively increased by 25% in *fmtclpc1* compared with *clpc1*, consistent with suppression of the
430 virescent phenotype (Supplemental Figure 5C). Consequently, relative investment in most other
431 functional categories decreased, except for gluconeogenesis/glyoxylate cycle (bin 6), nitrogen
432 metabolism (bin 12), and the TCA cycle/organic acid metabolism (bin 8), which increased by 9%,
433 4% and 3%, respectively. The relative abundance of the chloroplast ClpPRT complex was slightly
434 lower (18%), whereas ClpC2 was 36% higher in *fmtclpc1* compared with *clpc1-1* (ClpC1 was not
435 detected) (Fig. 5A), consistent with increased *CLPC2* RNA levels (Fig. 3D).

436 Figure 5B shows the volcano plot of individual proteins comparing the two genotypes. At P<0.01
437 and a >2-fold difference between genotypes, 13 proteins increased and 32 decreased in *fmtclpc1*
438 compared with *clpc1* (Fig. 5B, Table 1). All 13 increased proteins were plastid (8) or mitochondrial
439 (4), except for REDUCED CHLOROPLAST COVERAGE 2 (REC2), which is localized to the

440 cytosol. REC2 was enriched 2.3-fold in the double mutant. REC2 has two homologs (REC1 and
441 REC3), and the REC family is phylogenetically related to FMT. REC1 and REC3 were detected
442 in both genotypes, whereas FMT was detected only in *clpc1-1* and not in *fmtclpc1-1*, consistent
443 with *fmt* being a null line; REC1 and REC3 did not change significantly (Fig. 5C).

444 Six of the increased chloroplast proteins are directly involved in the light reactions of
445 photosynthesis, consistent with suppression of the virescent *clpc1* leaf phenotype. One additional
446 chloroplast protein is involved in chlorophyll synthesis, whereas the thylakoid rhodanese domain
447 protein has no known function. The mitochondrial protein showing the largest increase (4.6-fold)
448 was stomatin-like protein 1 (SLP1), localized to the inner mitochondrial membrane (Fig. 5B, Table
449 1). SLP1, likely together with its homolog SLP2, forms a ~3-MDa large complex in Arabidopsis
450 mitochondria (Gehl *et al.*, 2014). SLP2 was also strongly increased (6.7-fold) in *fmtclpc1* relative
451 to *clpc1* (p-value 0.013). SLP1 and SLP2 are part of the band-7/SPFH superfamily of membrane
452 scaffold proteins (Gehl and Sweetlove, 2014). Loss of SLP1 reduces protein abundance and
453 activity of respiratory complex I, indicating a role in its assembly and/or stability (Gehl *et al.*,
454 2014).

455 We also identified four mitochondrial prohibitins (PHB1, PHB2, PHB3, and PHB6), which are
456 members of the same superfamily (Gehl and Sweetlove, 2014); however, their abundance was not
457 increased in *fmtclpc1* compared with *clpc1*. Three additional mitochondrial proteins were
458 increased: the membrane transporter ATM3, which exports oxidized glutathione; galactonolactone
459 dehydrogenase (GLDH), which catalyzes the final step in ascorbate synthesis; and MTLPD1, a
460 redox-regulated enzyme involved in photorespiration and the TCA cycle. These proteins are likely
461 upregulated in response to mitochondrial dysfunction and stress resulting from loss of FMT. The
462 ability of ATM3 to export GSSG has been implicated in helping to stabilize against excessive
463 glutathione oxidation in mitochondria and thereby maintaining a suitable redox potential (Marty
464 et al., 2019).

465 The 32 reduced proteins (*fmtclpc1* compared with *clpc1*) were distributed across chloroplasts (14),
466 mitochondria (3), or other cellular compartments, encompassing diverse functions, particularly
467 plastid fatty acid and lipid metabolism and plastid RNA-related processes (Table 1). The most

468 strongly decreased proteins included FMT (as expected), cytosolic HSP90-1 involved in protein
469 folding, the chloroplast thylakoid protein LIL1.2/ELIP2 (Tzvetkova-Chevolleau et al., 2007), the
470 chloroplast pyruvate dehydrogenase E1-β subunit (PDH-Eβ) involved in acetyl-CoA synthesis for
471 fatty acid biosynthesis, a chloroplast DEAD/DEAH-box helicase of unknown function, the
472 essential mitochondrial intermembrane space protein TIM10 involved in protein sorting, and the
473 chloroplast inner envelope pyruvate importer BASS2 (Furumoto et al., 2011). LIL1.2/ELIP2
474 reduces chlorophyll levels by inhibiting chlorophyll synthesis rather than increasing chlorophyll
475 degradation, and LIL1.2/ELIP2 does not directly affect photosystem function or the electron
476 transport chain (Tzvetkova-Chevolleau *et al.*, 2007). Its low ratio (0.19) in *fmtclpc1/clpc1* is
477 consistent with the low chlorophyll levels observed in *clpc1*. HSP90-1 is a cytosolic member of
478 the large HSP90 family (7 members) of protein chaperones involved in protein folding, maturation,
479 and degradation. HSP90-1 was reduced six-fold in *fmtclpc1* compared with *clpc1* (Fig. 5B, Table
480 1), indicating that cytosolic folding demand is higher in *clpc1* than in the double mutant. We
481 identified all seven HSP90 members (HSP90-1 to -7), including chloroplast cpHSP90-5,
482 mitochondrial HSP90-6 and ER-localized HSP90-7, as well as the four cytosolic members
483 (HSP90-1 to -4) (Fig. 5D). All HSP90 members were lower in *fmtclpc1* than *clpc1,* indicating that
484 suppression of *clpc1* resulted in reduced folding stress (or demands) across subcellular
485 compartments (Wu et al., 2019).

486 **REC1 and REC2 are required for full suppression of the *clpc1-1* phenotype by *fmt***

487 In both our RNA-seq-based transcriptomic and MS/MS-based proteomic analyses, REC2 mRNA
488 and protein were induced during *fmt*-mediated suppression of *clpc1-1*. Given its close phylogenetic
489 relationship to *FMT*, we prioritized *REC2* together with its paralogs *REC1* and *REC3* for follow-
490 up functional analysis. RT–qPCR (Fig. 6A) confirmed the RNA-seq results and was consistent
491 with the proteomic analysis (Fig. 5C). *REC2* was increased 2.5-fold in *fmt-3clpc1-1*, and decreased
492 to 0.6-fold in *FMT/clpc1-1* (OE#1), both relative to *clpc1-1* (Fig. 6A). In contrast, *REC1* and *REC3*
493 transcript levels were largely unchanged, indicating that *REC2* is the only REC family member
494 responsive to loss of *FMT* function.

495 We next tested whether *REC1*, *REC2*, or *REC3* might share *FMT*'s capacity to suppress the *clpc1-*
496 *1* phenotype. To address this, we generated double mutants between *clpc1-1* and *rec1-3*, *rec2-1*,
497 or *rec3-1*. As shown in Figure 6B, none of these double mutants exhibited suppression of the *clpc1-*
498 *1* phenotype. The *rec3-1clpc1-1* mutant closely resembled *clpc1-1* alone, whereas both *rec1-*
499 *3clpc1-1* and *rec2-1clpc1-1* displayed smaller rosettes and more pronounced chlorosis than *clpc1-*
500 *1*. These results indicate that, although evolutionarily related to *FMT*, the *REC* genes cannot
501 substitute for *FMT* function in mitigating *CLPC1* deficiency.

502 We next tested whether *REC* genes are required for *fmt*-mediated rescue. Both *fmt-3rec1-3clpc1-*
503 *1* and *fmt-3rec2-1clpc1-1* exhibited intermediate phenotypes between *fmt-3clpc1-1* and *clpc1-1*,
504 whereas *fmt-3rec3-1clpc1-1* resembled *fmt-3clpc1-1* (Fig. 6C). Pigment analyses mirrored these
505 patterns: total chlorophyll and carotenoids were reduced in *fmt-3rec1-3clpc1-1* and *fmt-3rec2-*
506 *1clpc1-1* relative to *fmt-3clpc1-1*, while *fmt-3rec3-1clpc1-1* remained unchanged (Fig. 6D).
507 *CLPC2* transcript abundance followed the same trend—reduced in *fmt-3rec1-3clpc1-1* and *fmt-*
508 *3rec2-1clpc1-1*, unchanged in *fmt-3rec3-1clpc1-1* (Fig. 6E). Together, these results show that
509 *REC1* and *REC2* are required for full *fmt*-mediated suppression of *clpc1-1*, whereas *REC3* is
510 dispensable. *REC1* appears to be constitutively expressed, while *REC2* is upregulated in response
511 to the loss of *FMT*.

512

513 **DISCUSSION**

514 Our study reveals an unexpected connection between mitochondrial dysfunction and chloroplast
515 proteostasis, showing that loss of *FMT*–a regulator of mitochondrial morphology (El Zawily *et al.*,
516 2014; Logan *et al.*, 2003)—enables a compensatory response that restores chloroplast function in
517 the absence of ClpC1. Although *fmt* mutants exhibit clustered mitochondria and impaired
518 mitochondrial dynamics, they paradoxically display improved chloroplast performance in the
519 *clpc1* background. These findings indicate that mitochondrial perturbation in *fmt* does not simply
520 exacerbate cellular stress but is associated with selective transcriptional and proteomic changes—

521 most notably induction of *CLPC2*—that enable functional compensation for loss of ClpC1. A
522 working model summarizing these contrasting cellular states is presented in Fig. 6F,G.

523 In the *clpc1* mutant (Fig. 6F), loss of ClpC1 establishes a plastid stress state associated with plastid-
524 to-nucleus retrograde signaling and a broadly repressive nuclear response. This state correlates
525 with reduced expression of transcription factors such as GLK1 and BBX15 and decreased
526 expression of photosynthesis-related genes. In parallel, plastid-localized metabolic response genes
527 including *ACC2* are upregulated, reflecting altered plastid metabolic status linked to impaired
528 chloroplast proteostasis and the small, virescent phenotype. Together, these features define a
529 stress-associated transcriptional configuration that is insufficient to restore plastid function.

530 By contrast, loss of FMT shifts the system into a recovery state (Fig. 6G). Despite persistent
531 mitochondrial clustering, *fmt*-mediated suppression restores chloroplast ultrastructure,
532 photosynthetic protein accumulation, and Clp-dependent proteolysis. This transition correlates
533 with induction of *REC2* and derepression of *CLPC2*, enabling ClpC2 to functionally substitute for
534 ClpC1. In this recovery state, transcription factors associated with chloroplast gene programs,
535 including GLK1 and BBX15, are restored, photosynthesis-related genes are reactivated, and
536 plastid stress markers such as *ACC2* and *ELIP2* decline. These changes occur independently of
537 GUN1-dependent retrograde signaling, indicating engagement of a distinct mitochondria-to-
538 nucleus communication route rather than canonical plastid stress pathways. Although GUN1 is
539 known to buffer import-associated defects (Wu *et al.*, 2019) and to stabilize specific plastid RNAs
540 to maintain organellar gene expression (Tang *et al.*, 2024), these responses alone are insufficient
541 to restore chloroplast function in *clpc1*. The ability of *fmt* to suppress *clpc1* in the absence of GUN1,
542 together with the persistence of mitochondrial abnormalities in suppressed lines, indicates that
543 mitochondrial perturbation promotes plastid recovery through a mechanism distinct from
544 established plastid-to-nucleus signaling pathways.

545 The recurrence and strength of *fmt* alleles among independent suppressors highlight a specific role
546 for FMT in enabling compensation for ClpC1 loss. Although additional suppressor lines were
547 recovered in the screen, none displayed the near-complete phenotypic restoration observed in *fmt*
548 mutants, underscoring the distinctive contribution of *FMT*. Loss of *FMT* does not mitigate defects

549 in other components of the Clp protease system (Kim *et al.*, 2015; Rudella *et al.*, 2006) or
550 chloroplast protein import (Bedard *et al.*, 2017; Kubis *et al.*, 2003), further emphasizing that the
551 compensatory response is not a general bypass of plastid dysfunction.

552 A key downstream effector of this compensatory transition is *CLPC2*, a ClpC1 paralog. While
553 ClpC2 plays a minor role under normal conditions (Kovacheva *et al.*, 2007; Nishimura *et al.*, 2013)
554 and has been implicated in responses to organelle perturbation (Lopez *et al.*, 2024), our data extend
555 this view by showing that mitochondrial perturbation is sufficient to drive *CLPC2* transcription to
556 levels that restore Clp-dependent proteolysis and chloroplast biogenesis. The proportional
557 increases in *CLPC2* expression observed in native-promoter overexpression lines indicate that the
558 promoter is not saturated in *clpc1-1*, suggesting that *fmt* derepresses *CLPC2*. Conversely,
559 increasing *FMT* abundance reduces *CLPC2* expression and produces phenotypes resembling the
560 *clpc1-1clpc2-2* double mutant, consistent with an indirect, dose-dependent negative influence of
561 *FMT* on *CLPC2* expression.

562 The integrated RNA-seq and comparative proteomics analyses provide critical context for this
563 genetic compensation. Rather than revealing activation of a dominant stress or retrograde signaling
564 pathway, these datasets show coordinated remodeling of nuclear gene expression and chloroplast
565 protein investment in *fmtclpc1*. Transcriptome profiling indicates partial restoration of
566 photosynthesis-associated gene expression and attenuation of plastid proteotoxic stress signatures,
567 accompanied by selective remodeling of stress- and signaling-associated gene clusters. Notably,
568 Cluster III highlights genes involved in hormonal (JA- and SA-related) and metabolic adjustment
569 that are selectively enriched in *fmtclpc1*, supporting the idea that suppression involves entry into a
570 distinct adaptive cellular state rather than engagement of a linear signaling cascade. Comparative
571 proteomics reinforces this interpretation by demonstrating recovery of chloroplast protein
572 accumulation and reduced cytosolic chaperone burden, consistent with improved plastid function
573 rather than a generalized stress response.

574 Genetic and proteomic analyses further implicate REC proteins in linking mitochondrial
575 perturbation to *CLPC2* induction. *REC2* is strongly enriched in *fmtclpc1*, and both *REC1* and
576 *REC2* are required for full *fmt*-mediated suppression, whereas *REC3* appears dispensable.

577 Together with previous studies showing roles for REC proteins in plastid compartment size (Hu *et*
578 *al.*, 2024; Larkin *et al.*, 2016) and plastid-related gene expression (Hu *et al.*, 2024), our findings
579 support a model in which *REC1* and *REC2* act genetically upstream of *CLPC2* induction and
580 contribute to the broader remodeling of plastid proteostasis during the transition from the *clpc1*
581 stress state to the *fmt*-mediated recovery state.

582 Previous work has identified GOLDEN2-LIKE and B-BOX transcription factors as components
583 of transcriptional networks linking chloroplast functional status with nuclear gene regulation
584 (Susila et al., 2023). In our study, *GLK1* and *BBX15* showed genotype-dependent expression
585 changes across *clpc1*, *fmt*, and *fmtclpc1*, consistent with their placement within the two-state model
586 outlined in Fig. 6F,G. By contrast, GLK2, BBX14, and BBX16 did not exhibit coordinated
587 expression changes, suggesting context-dependent engagement of the GLK–BBX regulatory
588 network.

589 Together, these findings support a model in which mitochondrial perturbation exposes a latent
590 capacity for inter-organelle compensation, enabling selective transcriptional and proteomic
591 remodeling that restores chloroplast proteostasis when ClpC1 function is compromised. Rather
592 than simply alleviating stress, loss of FMT appears to shift the cellular signaling landscape from a
593 repressive plastid stress state to a compensatory recovery state.

594 **MATERIALS AND METHODS**

595 **EMS Mutagenesis and Suppressor Mapping by Whole-Genome Sequencing**

596 Approximately 10,000 *Arabidopsis thaliana clpc1-1* seeds (Col-0 background) were subjected to
597 ethyl methanesulfonate (EMS) mutagenesis following standard procedures (Kim et al., 2006).
598 Treated seeds (M1 generation) were sown on soil and grown under long-day conditions (16/8 hour
599 light/dark cycle at 100 µmol photons m^{-2} s^{-1}, 22 °C). M2 seeds were collected in bulk from
600 individual M1 plants and screened for suppressor phenotypes. The *clpc1-1* mutant exhibits a strong
601 chlorotic and stunted phenotype, allowing visual identification of M2 seedlings with restored leaf
602 greening and improved growth. Approximately 60 groups of M2 seedlings were examined, and
603 ~10 independent suppressor candidates showing partial or near-complete phenotypic recovery
604 were identified. Four lines exhibiting the strongest recovery were selected for further analysis and
605 designated *socc* (*suppressor of clpc1*). Each *socc* line was backcrossed to the parental *clpc1-1*
606 mutant to generate BC1F2 populations. Segregation of the suppressor phenotype among BC1F2
607 progeny followed an approximate 1:3 ratio (green:chlorotic), consistent with monogenic recessive
608 inheritance.

609 For bulked segregant analysis, leaf tissue from at least 50 green and 50 chlorotic BC1F2 plants
610 was harvested separately. Genomic DNA was extracted using the DNeasy Plant Mini Kit (Qiagen),
611 and DNA from plants of the same phenotype was pooled to generate "green" and "chlorotic" bulks.
612 Whole-genome sequencing (WGS) was performed by BGI Genomics (Hong Kong). Candidate
613 causal variants were identified by comparing allele frequency differences between the green and
614 chlorotic bulks using the SIMPLE pipeline (Wachsman *et al.*, 2017). Putative causal mutations
615 were further validated by genetic complementation.

616 **Plant Growth, T-DNA Mutant Isolation, and RNA Preparation and RT-PCR Analysis**

617 Plant growth, genotyping, and RNA extraction were performed as described previously (Kim *et*
618 *al.*, 2009). Various growth conditions are detailed in the figure legends. All T-DNA insertion lines
619 were in the Columbia background and are as follows: *FMT* (AT3G52140), SALK_046271 (*fmt-3*)
620 and SALK_056717 (*fmt-4*); *CLPC1* (AT5G50920), SALK_014058 (*clpc1-1*); *CLPC2*

621 (AT3G48870), SAIL_622_B05 (*clpc2-2*); *CLPR2* (AT1G12410), SALK_046378 (*clpr2-1*);
622 *CLPT1* (AT4G25370), GK-285A05 (*clpt1-2*); *CLPT2* (AT4G12060), SAIL_340A10 (*clpt2-1*);
623 *TOC33* (AT1G02280), N2107726 (*ppi1-1*); *TIC40* (AT5G16620), SAIL_92_C10 (*tic40-4*); *GUN1*
624 (AT2G31400), SAIL_33_D01 (*gun1-101*); *REC1* (AT1G01320), SALK_049453C (*rec1-3*);
625 *REC2* (AT4G28080), SALK_020337C (*rec2-1*); and *REC3* (AT1G15290), SAIL_1164_H02
626 (*rec3-1*).

627 For RNA-seq analysis, total RNA was isolated using the RNeasy Plant Mini Kit (Qiagen). For RT-
628 PCR, total RNA was isolated using either the RNeasy Plant Mini Kit (Qiagen) or the XENOPURE
629 Total RNA Purification Kit (CelltoBio). First-strand cDNA was synthesized from equal amounts
630 of total RNA using SuperScript III Reverse Transcriptase (Invitrogen) or TOPscript Reverse
631 Transcriptase (Enzynomics). Semi-quantitative RT-PCR and RT-qPCR were performed as
632 described previously (Bae et al., 2025; Kim *et al.*, 2015). Graphs were generated using GraphPad
633 Prism 10. Primers used for genomic PCR, RT-PCR analysis, and various complementation assays
634 are listed in table S2.

635 **Cloning and Complementation**

636 For *FMT*, the full-length native promoter and 5′UTR of *FMT* (1.0 kb), together with the full-length
637 *FMT* genomic DNA (8.0 kb), totaling 9.0 kb, were PCR-amplified using KOD polymerase
638 (TOYOBO). The PCR products were cloned into a modified pCR8/GW/TOPO vector (Invitrogen),
639 into which BamHI and NotI restriction sites were introduced. Using LR Clonase (Invitrogen), the
640 DNA fragment was transferred into the pGWB4 Gateway destination plant binary vector. For
641 *CLPC2*, the full-length native promoter and 5′UTR of *CLPC2* (1.9 kb), together with the full-
642 length *CLPC2* genomic DNA (5.6 kb), totaling 7.5 kb, were PCR-amplified using KOD
643 polymerase (TOYOBO). The PCR products were cloned into a modified pCR8/GW/TOPO vector
644 (Invitrogen), into which PstI and NotI restriction sites, as well as a StrepII tag and a *nosT* sequence
645 (0.5 kb), were introduced. Using LR Clonase (Invitrogen), the DNA fragment was transferred into
646 the pMDC99 Gateway destination plant binary vector. The primers used are listed in table S2.
647 Competent cells of *Agrobacterium tumefaciens* strain GV3101 were transformed with the binary
648 vectors. Plant transformation and selection were performed as described previously (Kim *et al.*,

649 2009), using the *Agrobacterium*-mediated floral dip method with selection on ½ MS agar plates
650 containing 25 µg/mL hygromycin (Duchefa Biochemie). Complemented lines were identified and
651 verified by PCR genotyping.

652 **Generation of Mutant Lines Using CRISPR/Cas9**

653 Mutations in *CLPC1* were generated using the CRISPR/Cas9 system. sgRNAs were designed with
654 CRISPR-P v2.0 and cloned into the pBR-Cas9 vector (provided by Dr. Jae-Young Yun, SeoulTech,
655 Seoul, Korea). *Arabidopsis thaliana* Col-0 plants were transformed by the Agrobacterium-
656 mediated floral dip method (*A. tumefaciens* GV3101). Transgenic plants were screened by PCR
657 amplification of the target region followed by Sanger sequencing of CTAB-extracted DNA. Two
658 independent knockout alleles were recovered: *clpc1-4*, carrying a 1-bp insertion in exon 4, and
659 *clpc1-5*, containing a 32-bp deletion plus a single-nucleotide substitution in the same exon. Both
660 mutations introduce frameshifts predicted to abolish ClpC1 protein function. Cas9-free
661 homozygous segregants were identified by PCR-based genotyping (primer sequences in table S2)
662 and used for all subsequent analyses.

663 **Pigment Analysis**

664 Chlorophyll and carotenoid contents on a fresh-weight basis were measured in 80% acetone as
665 described previously (Kim *et al.*, 2013).

666 **Photosynthetic Efficiency Analysis**

667 Fv/Fm measurements were performed as described previously (Bae *et al.*, 2025). Briefly, plants
668 were dark-adapted for 30 min at room temperature, and chlorophyll fluorescence parameters (Fo
669 and Fm) were recorded using a FluorCam 800MF (Photon Systems Instruments, Czech Republic).
670 Fv/Fm values were calculated as (Fm - Fo)/Fm to evaluate photosystem II photochemical
671 efficiency under normal growth conditions.

672 **Transmission Electron Microscopy (TEM)**

673 Leaves from 23-day-old plants were fixed with a mixture of 2% (v/v) glutaraldehyde and 2% (v/v)
674 paraformaldehyde in 0.05 M cacodylate buffer (pH 7.2) at room temperature for 4 h. The samples
675 were washed with the same buffer and post-fixed with 1% (w/v) OsO_4 in 0.05 M cacodylate buffer
676 at room temperature for 1 h. Fixed samples were washed again with the buffer and dehydrated
677 through a graded ethanol series (30–100%). The samples were then embedded in LR White resin
678 at 50 °C for 24 h. Ultrathin sections (80–100 nm thick) were prepared using an ultramicrotome
679 equipped with a diamond knife. Sections were stained with uranyl acetate and lead citrate and
680 examined using a transmission electron microscope (JEM-2100F, JEOL Ltd., Japan).

681 **Chloroplast Isolation and Total Leaf Protein Extraction**

682 For chloroplast isolation, leaves from wild-type and various mutant alleles were briefly
683 homogenized in grinding medium (50 mM HEPES-KOH, pH 8.0, 330 mM sorbitol, 2 mM EDTA,
684 5 mM ascorbic acid, 5 mM cysteine, and 0.03% BSA) and filtered through a nylon mesh. The
685 crude plastids were collected by centrifugation at 1,100 g for 2 min and further purified on 35–85%
686 Percoll cushions (Percoll in 0.6% Ficoll and 1.8% polyethylene glycol) by centrifugation at 3,750
687 g for 10 min, followed by one additional wash in grinding medium lacking ascorbic acid, cysteine,
688 and BSA. Chloroplasts were subsequently lysed in 10 mM HEPES-KOH, pH 8.0, 5 mM $MgCl_2$,
689 and 15% glycerol, containing a mixture of protease inhibitors, under mild mechanical disruption.
690 Protein concentrations were determined using the BCA Protein Assay Kit (Thermo Scientific).
691 Total leaf proteins were extracted as described previously (Kim *et al.*, 2015).

692 **Immunoblot Analysis**

693 For immunoblotting, proteins were transferred onto nitrocellulose or polyvinylidene fluoride
694 (PVDF) membranes and probed with specific antibodies using chemiluminescence detection,
695 following standard procedures. The antisera against *Arabidopsis* ClpF and ClpS1 were described

696 previously (Nishimura *et al.*, 2015). The anti-PAA2 antibody was kindly provided by Dr. Marinus
697 Pilon (Colorado State Univ., Fort Collins, CO, USA).

698 **PAA2 Degradation Assay**

699 The PAA2 degradation assay was performed as described previously (Tapken *et al.*, 2015) with
700 minor modifications. Briefly, *Arabidopsis thaliana* seedlings were grown on half-strength MS agar
701 plates (pH 5.8) containing 0.6% (w/v) agar and 1% (w/v) sucrose for 21 days under short-day
702 conditions (10/14 hour light/dark cycle at 100 μmol photons m^{-2} s^{-1}). For copper treatments, 5 μM
703 $CuSO_4$ was added to the growth medium, and for control conditions, 0.05 μM $CuSO_4$ was used.
704 Total leaf protein extraction and immunoblot analysis were performed as described previously
705 (Kim *et al.*, 2015). PAA2 abundance was detected using affinity-purified anti-PAA2 antibodies
706 (1:1000 dilution).

707 **RNAseq analysis**.

708 RNA analysis was carried out for five genotypes of Arabidopsis seedlings in stage 1.07, with 3
709 biological replicates. The genotypes are: WT, *clpc1-1*, *fmt-3*, *fmt-3 clpc1-1*, FMT overexpressed
710 line OE#1 in *clpc1-1* (*FMT/clpc1*). Total RNA was isolated with an RNeasy plant mini kit
711 (Qiagen). Total RNA samples were processed for library preparation and sequencing following
712 the manufacturer's protocol. Briefly, mRNA was enriched from total RNA using oligo(dT) beads
713 targeting the poly(A) tails. The isolated mRNA was then fragmented into smaller pieces, which
714 served as templates for first-strand cDNA synthesis using random primers. Subsequently, second-
715 strand cDNA synthesis was performed, incorporating dUTP in place of dTTP to enable strand
716 specificity. The resulting double-stranded cDNA underwent end-repair and 3′-adenylation, after
717 which sequencing adapters were ligated. The adapter-ligated fragments were then amplified via
718 PCR, and the amplified libraries were subjected to quality control assessment. Following quality
719 control, the libraries were circularized and further amplified to form DNA nanoballs (DNBs).
720 Finally, sequencing was performed using the DNBSEQ platform (DNBSEQ Technology). Raw
721 data with adapter sequences or low-quality sequences was filtered using SOAPnuke (Chen et al.,

722 2018). For individual replicate-level expression analyses, the HISAT2 aligned bam files were used
723 for reads counting using the featureCounts program (Liao et al., 2014)

724 Data normalization (Supplemental Data Set 1A), downstream analysis of differentially expressed
725 genes, and adjusted p-value calculation were performed using the DESeq2 package v.1.44.0 (Love
726 et al., 2014) in R v4.4.3. . Specifically, a DESeqDataSet object was generated using the raw counts,
727 with design = ~genotype. Pairwise results for each genotypic comparison of interest were then
728 generated using the 'results()' function of DESeq2, with the function's contrast parameter being
729 used to specify the relevant genotypes. The p-values were determined by the default Wald test,
730 and these p-values were adjusted using the Benjamini-Hochberg method. Genes with a differential
731 expression of at least two-fold ($x<0.5$ or $x>2$) and adjusted p value <0.01 in one of the 10 possible
732 comparisons across genotypes were considered for further investigation. This resulted in a set of
733 4745 nuclear protein-coding genes that we annotated for subcellular protein location (in particular
734 chloroplast and mitochondria) and function (using the MapMan bin system) from public resources
735 (TAIR, PPDB and publications) (Supplemental Data Set 1B). The gene clustering was generated
736 using the Ward D2 method with Euclidean distance in the pheatmap v1.0.13 R package
737 (Supplemental Data Set 1B). PCA analysis was performed using the GLEE software (Kim *et al.*,
738 2013). The graphs are generated either using Microsoft Excel or GraphPad Prism 10.

739 **Comparative Proteome Analysis**

740 Total proteome extracts of seedlings of *clpc1-1* and *fmt-3 clpc1-1* (each with three biological
741 replicates) were separated by Tris-Glycine SDS-PAGE using 8-16% precast gels (Cat. No.
742 KG7550-BC; KOMA Biotech, Korea). Gels were stained with Coomassie Brilliant Blue. Each of
743 the six SDS-PAGE gel lanes was completely cut into consecutive gel slices (10 slices per lane),
744 followed by reduction, alkylation, and in-gel digestion with trypsin as described in (Friso et al.,
745 2011). The extracted peptides were resuspended in 2% formic acid and analyzed using a QExactive
746 mass spectrometer equipped with a nanospray flex ion source and interfaced with a nanoLC system
747 and autosampler (Dionex Ultimate 3000 Binary RSLCnano system) as described in (Rei Liao *et*
748 *al.*, 2022) with the exception that AGC target values were set at 1×10^6 for the MS survey scans
749 and maximum scan time 30 ms and 5×10^5 for MSMS scans and maximum scan time 50 ms [Other

750 parameters: MS: 70k resolution, scan range 400-2000 m/z; MSMS: 17.5k resolution, top10, loop
751 count 10, isolation window 2.0 m/z, dynamic exclusion 15 sec].

752 Peak lists in MGF format were generated from RAW files using Distiller software (version 2.7.1.0)
753 in default mode (Matrix Science). MGF files were searched with MASCOT v2.4.0 against TAIR10
754 including a set of typical contaminants and the decoy (71148 sequences; 29099536 residues). Two
755 parallel searches (Mascot p-value <0.01 for individual ion scores; precursor ion window 700 to
756 3500 Da) were carried out: (i) Full tryptic (error tolerance 10 ppm for MS and 0.5 Da for MS/MS)
757 and (ii) Semi-tryptic (error tolerance 6 ppm and 0.5 Da for MS/MS) in both cases with fixed Cys-
758 carbamido-methylation and variable M-oxidation, N-terminal acetylation, N-terminal formylation
759 and 2 missed cleavages (in Mascot PR or PK does not count as missed cleavage). In-house post-
760 Mascot filtering removed redundancies between the full and semi-tryptic searches and removed
761 spectral matches with ion scores below 33. Proteins could only be identified by the spectral
762 counting method (SPC) with the full tryptic (6 ppm) search. The semi-tryptic search served to
763 increase protein coverage and was combined with the full tryptic search results. Final false
764 discovery rate for proteins identified with one spectral match was zero for those with two or more
765 spectral matches. Proteins identified by MS/MS spectra that were all shared with other proteins
766 identified by unique peptides were discarded.

767 Proteins were quantified by the spectral counting method (SPC) using full and semi-tryptic
768 peptides search results. For quantification by spectral counting, each accession was scored for total
769 spectral counts (SPC), unique SPC (uniquely matching to an accession) and adjusted SPC (Friso
770 *et al.*, 2011). The latter assigns shared peptides to accessions in proportion to their relative
771 abundance using unique spectral counts for each accession as a basis. Proteins that shared more
772 than 80% of their matched peptides with other proteins across the complete dataset were grouped
773 into families quantified as groups with these homologs (Friso *et al.*, 2011). After selecting only
774 the best scoring isoform model per protein, proteins that shared a significant number of matched
775 spectra were grouped, and proteins and groups with less than 3 adjSPC were discarded for further
776 analysis; this resulted in 2976 proteins including 124 groups. For significance analysis and
777 Volcano plots to compare the two genotypes, the minimal total adjSPC was raised to >12, resulting
778 in 1529 proteins and groups; this ensured a more robust dataset and lower FDR. Within each

779 sample, a value of 0.99 AdjSPC was imputed for all proteins with missing values. This was
780 followed by normalization of the adjSPC to the total adjSPC of the samples resulting in NadjSPC
781 for each protein. Average NadjSPC per genotype across the 3 replicates were calculated and
782 *fmtclpc1/clpc1* NadjSPC ratios were determined for each protein. p-value and q-value (FDR) were
783 then calculated to determine proteins that showed significant abundance differences between *clpc1*
784 and *fmtclpc1*. We created Volcano plots and plotted total protein abundance against the protein
785 abundance ratios.

786 **ACKNOWLEDGMENTS**

787 This research was supported by the following grants: National Research Foundation of Korea
788 (2019R1I1A1A01064009 and RS-2023-00247582 to J.K., RS-2023-00208784 to D.W.L., RS-
789 2024-00407469 and RS-2025-00564152 to B.h.L., and NRF-2022R1A3B1078180 to J.H.A.), and
790 a US National Science Foundation grant MCB-2322813 to K.J.v.W.

791 **AUTHOR CONTRIBUTIONS**

792 J.K. conceived the experiments, and K.J.v.W. conceived the multi-omics experiments. J.K.
793 performed EMS screening, all genetic crosses, and data analysis. K.J.v.W. and P.R. performed
794 quantitative comparative proteomics and RNA-seq analyses, while Z.N. conducted the initial
795 RNA-seq analysis. N.S. and H.L. provided bioinformatics consultation and support. J.K., C.N.,
796 and D.B.K. performed biochemical experiments, including total and chloroplast protein
797 extraction and immunoblotting. J.K., D.B.K., and J.-Y.K. performed cloning. C.N. carried out
798 the PAA2 degradation assay, and J.-Y.K. generated CRISPR/Cas9 lines. J.K., N.B., and H.K.
799 performed RT-PCR analyses. J.K. prepared samples for RNA-seq and proteomics. J.K., C.N.,
800 N.B., H.K., D.B.K., R.L., J.H.K., and G.C. performed plant transformation and/or other
801 molecular genetic experiments. J.K., J.H.A., B.h.L., D.W.L., and K.J.v.W. supervised the project
802 and analyzed and interpreted the data. J.K. and K.J.v.W. wrote the manuscript. D.W.L. and P.R.
803 reviewed, edited, and provided substantive feedback on the manuscript. C.N., N.B., H.K., J.-
804 Y.K., D.B.K., N.S., Z.N., R.L., J.H.K., G.C., H.L., and B.h.L. reviewed the manuscript and
805 provided additional comments and/or editorial suggestions.

806 **COMPETING INTERESTS:** Authors declare that they have no competing interests.

807 **DATA AND MATERIALS AVAILABILITY**

808 MS-based protein identifications are available through the Plant Proteome Data Base (PPDB)
809 under experiment ids #2599-2604. MS-based protein quantifications are available in the
810 Supplemental Data Sets. RNA-seq data are available in the GEO repository under accession
811 number GSE307303

812 **SUPPLEMENTAL INFORMATION**

813 Supplemental Figures 1-5

814 Supplemental Tables 1-3

815 Supplemental Data Sets 1 and 2

REFERENCES

Atanasov, V., Schumacher, J., Muino, J.M., Larasati, C., Wang, L., Kaufmann, K., Leister, D., and Kleine, T. (2024). Arabidopsis BBX14 is involved in high light acclimation and seedling development. Plant J **118**:141–158. 10.1111/tpj.16597.

Ayabe, H., Kawai, N., Shibamura, M., Fukao, Y., Fujimoto, M., Tsutsumi, N., and Arimura, S.I. (2021). FMT, a protein that affects mitochondrial distribution, interacts with translation-related proteins in Arabidopsis thaliana. Plant Cell Rep **40**:327–337. 10.1007/s00299-020-02634-9.

Bae, N., Shim, S.H., Alavilli, H., Do, H., Park, M., Lee, D.W., Lee, J.H., Lee, H., Li, X., Lee, C.H., et al. (2025). Enhanced salt stress tolerance in plants without growth penalty through increased photosynthesis activity by plastocyanin from Antarctic moss. Plant J **121**:e17168. 10.1111/tpj.17168.

Bedard, J., Trosch, R., Wu, F., Ling, Q., Flores-Perez, U., Topel, M., Nawaz, F., and Jarvis, P. (2017). Suppressors of the Chloroplast Protein Import Mutant tic40 Reveal a Genetic Link between Protein Import and Thylakoid Biogenesis. Plant Cell **29**:1726–1747. 10.1105/tpc.16.00962.

Bittner, A., Ciesla, A., Gruden, K., Lukan, T., Mahmud, S., Teige, M., Vothknecht, U.C., and Wurzinger, B. (2022). Organelles and phytohormones: a network of interactions in plant stress responses. J Exp Bot **73**:7165–7181. 10.1093/jxb/erac384.

Bouchnak, I., and van Wijk, K.J. (2021). Structure, function, and substrates of Clp AAA+ protease systems in cyanobacteria, plastids, and apicoplasts: A comparative analysis. J Biol Chem **296**:100338. 10.1016/j.jbc.2021.100338.

Brownfield, D.L., Todd, C.D., and Deyholos, M.K. (2008). Analysis of Arabidopsis arginase gene transcription patterns indicates specific biological functions for recently diverged paralogs. Plant Mol Biol **67**:429–440. 10.1007/s11103-008-9336-2.

Chen, Y., Chen, Y., Shi, C., Huang, Z., Zhang, Y., Li, S., Li, Y., Ye, J., Yu, C., Li, Z., et al. (2018). SOAPnuke: a MapReduce acceleration-supported software for integrated quality control and preprocessing of high-throughput sequencing data. Gigascience **7**:1–6. 10.1093/gigascience/gix120.

Chustecki, J.M., Etherington, R.D., Gibbs, D.J., and Johnston, I.G. (2022). Altered collective mitochondrial dynamics in the Arabidopsis msh1 mutant compromising organelle DNA maintenance. J Exp Bot **73**:5428–5439. 10.1093/jxb/erac250.

El Zawily, A.M., Schwarzlander, M., Finkemeier, I., Johnston, I.G., Benamar, A., Cao, Y., Gissot, C., Meyer, A.J., Wilson, K., Datla, R., et al. (2014). FRIENDLY regulates mitochondrial distribution, fusion, and quality control in Arabidopsis. Plant Physiol **166**:808–828. 10.1104/pp.114.243824.

Elhafez, D., Murcha, M.W., Clifton, R., Soole, K.L., Day, D.A., and Whelan, J. (2006). Characterization of mitochondrial alternative NAD(P)H dehydrogenases in Arabidopsis: intraorganelle location and expression. Plant Cell Physiol **47**:43–54. 10.1093/pcp/pci221.

Friso, G., Olinares, P.D., and van Wijk, K.J. (2011). The workflow for quantitative proteome analysis of chloroplast development and differentiation, chloroplast mutants, and protein interactions by spectral counting. Methods Mol Biol **775**:265–282. 10.1007/978-1-61779-237-3_14.

Furumoto, T., Yamaguchi, T., Ohshima-Ichie, Y., Nakamura, M., Tsuchida-Iwata, Y., Shimamura, M., Ohnishi, J., Hata, S., Gowik, U., Westhoff, P., et al. (2011). A plastidial sodium-dependent pyruvate transporter. Nature **476**:472–475. 10.1038/nature10250.

Gao, L.L., Hong, Z.H., Wang, Y., and Wu, G.Z. (2023). Chloroplast proteostasis: A story of birth, life, and death. Plant Commun **4**:100424. 10.1016/j.xplc.2022.100424.

Gao, Y., and Zhao, Y. (2013). Epigenetic suppression of T-DNA insertion mutants in Arabidopsis. Mol Plant **6**:539–545. 10.1093/mp/sss093.

Gehl, B., and Sweetlove, L.J. (2014). Mitochondrial Band-7 family proteins: scaffolds for respiratory chain assembly? Front Plant Sci **5**:141. 10.3389/fpls.2014.00141.

Gehl, B., Lee, C.P., Bota, P., Blatt, M.R., and Sweetlove, L.J. (2014). An Arabidopsis stomatin-like protein affects mitochondrial respiratory supercomplex organization. Plant Physiol **164**:1389–1400. 10.1104/pp.113.230383.

He, C., Berkowitz, O., Hu, S., Zhao, Y., Qian, K., Shou, H., Whelan, J., and Wang, Y. (2023). Co-regulation of mitochondrial and chloroplast function: Molecular components and mechanisms. Plant Commun **4**:100496. 10.1016/j.xplc.2022.100496.

Hemono, M., Salinas-Giege, T., Roignant, J., Vingadassalon, A., Hammann, P., Ubrig, E., Ngondo, P., and Duchene, A.M. (2022). FRIENDLY (FMT) is an RNA binding protein associated with cytosolic ribosomes at the mitochondrial surface. Plant J **112**:309–321. 10.1111/tpj.15962.

Hernandez-Verdeja, T. (2025). Regulation of Chloroplast Biogenesis and Differentiation. J Exp Bot 10.1093/jxb/eraf530.

Hu, Q., Zhang, H., Song, Y., Song, L., Zhu, L., Kuang, H., and Larkin, R.M. (2024). REDUCED CHLOROPLAST COVERAGE proteins are required for plastid proliferation and carotenoid accumulation in tomato. Plant Physiol **196**:511–534. 10.1093/plphys/kiae275.

Jia, X., Chanda, B., Zhao, M., Brunner, A.M., and Beers, E.P. (2015). Instability of the Arabidopsis mutant csn5a-2 caused by epigenetic modification of intronic T-DNA. Plant Sci **238**:53–63. 10.1016/j.plantsci.2015.05.015.

Kacprzak, S.M., and Van Aken, O. (2023). FRIENDLY is required for efficient dark-induced mitophagy and controlled senescence in Arabidopsis. Free Radic Biol Med **204**:1–7. 10.1016/j.freeradbiomed.2023.04.007.

Kim, J., Rudella, A., Ramirez Rodriguez, V., Zybailov, B., Olinares, P.D., and van Wijk, K.J. (2009). Subunits of the plastid ClpPR protease complex have differential contributions to embryogenesis, plastid biogenesis, and plant development in Arabidopsis. Plant Cell **21**:1669–1692. 10.1105/tpc.108.063784.

Kim, J., Olinares, P.D., Oh, S.H., Ghisaura, S., Poliakov, A., Ponnala, L., and van Wijk, K.J. (2013). Modified Clp protease complex in the ClpP3 null mutant and consequences for chloroplast development and function in Arabidopsis. Plant Physiol **162**:157–179. 10.1104/pp.113.215699.

Kim, J., Kimber, M.S., Nishimura, K., Friso, G., Schultz, L., Ponnala, L., and van Wijk, K.J. (2015). Structures, Functions, and Interactions of ClpT1 and ClpT2 in the Clp Protease System of Arabidopsis Chloroplasts. Plant Cell **27**:1477–1496. 10.1105/tpc.15.00106.

Kim, Y., Schumaker, K.S., and Zhu, J.K. (2006). EMS mutagenesis of Arabidopsis. Methods Mol Biol **323**:101–103. 10.1385/1-59745-003-0:101.

Kovacheva, S., Bédard, J., Wardle, A., Patel, R., and Jarvis, P. (2007). Further in vivo studies on the role of the molecular chaperone, Hsp93, in plastid protein import. Plant J. **50**:364–379. 10.1111/j.1365-313X.2007.03060.x.

Kubis, S., Baldwin, A., Patel, R., Razzaq, A., Dupree, P., Lilley, K., Kurth, J., Leister, D., and Jarvis, P. (2003). The Arabidopsis ppi1 mutant is specifically defective in the expression,

907 chloroplast import, and accumulation of photosynthetic proteins. Plant Cell **15**:1859–1871.
908 10.1105/tpc.012955.
909 **Lama, S., Broda, M., Abbas, Z., Vaneechoutte, D., Belt, K., Sall, T., Vandepoele, K., and Van**
910 **Aken, O.** (2019). Neofunctionalization of Mitochondrial Proteins and Incorporation into
911 Signaling Networks in Plants. Mol Biol Evol **36**:974–989. 10.1093/molbev/msz031.
912 **Larkin, R.M., Stefano, G., Ruckle, M.E., Stavoe, A.K., Sinkler, C.A., Brandizzi, F.,**
913 **Malmstrom, C.M., and Osteryoung, K.W.** (2016). REDUCED CHLOROPLAST
914 COVERAGE genes from Arabidopsis thaliana help to establish the size of the chloroplast
915 compartment. Proc Natl Acad Sci U S A **113**:E1116–1125. 10.1073/pnas.1515741113.
916 **Lee, K.P., Li, M., Li, M., Liu, K., Medina-Puche, L., Qi, S., Cui, C., Lozano-Duran, R., and**
917 **Kim, C.** (2023). Hierarchical regulatory module GENOMES UNCOUPLED1-GOLDEN2-
918 LIKE1/2-WRKY18/40 modulates salicylic acid signaling. Plant Physiol **192**:3120–3133.
919 10.1093/plphys/kiad251.
920 **Liao, Y., Smyth, G.K., and Shi, W.** (2014). featureCounts: an efficient general purpose program
921 for assigning sequence reads to genomic features. Bioinformatics **30**:923–930.
922 10.1093/bioinformatics/btt656.
923 **Llamas, E., and Pulido, P.** (2022). A proteostasis network safeguards the chloroplast proteome.
924 Essays Biochem **66**:219–228. 10.1042/EBC20210058.
925 **Logan, D.C., Scott, I., and Tobin, A.K.** (2003). The genetic control of plant mitochondrial
926 morphology and dynamics. Plant J **36**:500–509. 10.1046/j.1365-313x.2003.01894.x.
927 **Lopez, B., Izquierdo, Y., Cascon, T., Zamarreno, A.M., Garcia-Mina, J.M., Pulido, P., and**
928 **Castresana, C.** (2024). Mutant noxy8 exposes functional specificities between the
929 chloroplast chaperones CLPC1 and CLPC2 in the response to organelle stress and plant
930 defence. Plant Cell Environ **47**:2336–2350. 10.1111/pce.14882.
931 **Love, M.I., Huber, W., and Anders, S.** (2014). Moderated estimation of fold change and
932 dispersion for RNA-seq data with DESeq2. Genome Biol **15**:550. 10.1186/s13059-014-0550-
933 8.
934 **Ma, J., Liang, Z., Zhao, J., Wang, P., Ma, W., Mai, K.K., Fernandez Andrade, J.A., Zeng,**
935 **Y., Grujic, N., Jiang, L., et al.** (2021). Friendly mediates membrane depolarization-induced
936 mitophagy in Arabidopsis. Curr Biol **31**:1931–1944 e1934. 10.1016/j.cub.2021.02.034.
937 **Marty, L., Bausewein, D., Muller, C., Bangash, S.A.K., Moseler, A., Schwarzlander, M.,**
938 **Muller-Schussele, S.J., Zechmann, B., Riondet, C., Balk, J., et al.** (2019). Arabidopsis
939 glutathione reductase 2 is indispensable in plastids, while mitochondrial glutathione is
940 safeguarded by additional reduction and transport systems. New Phytol **224**:1569–1584.
941 10.1111/nph.16086.
942 **Morikawa, K., Shiina, T., Murakami, S., and Toyoshima, Y.** (2002). Novel nuclear-encoded
943 proteins interacting with a plastid sigma factor, Sig1, in Arabidopsis thaliana. FEBS Lett
944 **514**:300–304. 10.1016/s0014-5793(02)02388-8.
945 **Nakamura, S., Hagihara, S., Otomo, K., Ishida, H., Hidema, J., Nemoto, T., and Izumi, M.**
946 (2021). Autophagy Contributes to the Quality Control of Leaf Mitochondria. Plant Cell
947 Physiol **62**:229–247. 10.1093/pcp/pcaa162.
948 **Nishimura, K., Apitz, J., Friso, G., Kim, J., Ponnala, L., Grimm, B., and van Wijk, K.J.**
949 (2015). Discovery of a Unique Clp Component, ClpF, in Chloroplasts: A Proposed Binary
950 ClpF-ClpS1 Adaptor Complex Functions in Substrate Recognition and Delivery. Plant Cell
951 **27**:2677–2691. 10.1105/tpc.15.00574.

952 **Nishimura, K., Asakura, Y., Friso, G., Kim, J., Oh, S.H., Rutschow, H., Ponnala, L., and van**
953 **Wijk, K.J.** (2013). ClpS1 is a conserved substrate selector for the chloroplast Clp protease
954 system in Arabidopsis. Plant Cell **25**:2276–2301. 10.1105/tpc.113.112557.
955 **Ohmiya, A., Oda-Yamamizo, C., and Kishimoto, S.** (2019). Overexpression of CONSTANS-
956 like 16 enhances chlorophyll accumulation in petunia corollas. Plant Sci **280**:90–96.
957 10.1016/j.plantsci.2018.11.013.
958 **Olinares, P.D., Kim, J., Davis, J.I., and van Wijk, K.J.** (2011). Subunit stoichiometry, evolution,
959 and functional implications of an asymmetric plant plastid ClpP/R protease complex in
960 Arabidopsis. Plant Cell **23**:2348–2361. 10.1105/tpc.111.086454.
961 **Paila, Y.D., Richardson, L.G.L., and Schnell, D.J.** (2015). New insights into the mechanism of
962 chloroplast protein import and its integration with protein quality control, organelle
963 biogenesis and development. J Mol Biol **427**:1038–1060. 10.1016/j.jmb.2014.08.016.
964 **Rei Liao, J.Y., Friso, G., Forsythe, E.S., Michel, E.J.S., Williams, A.M., Boguraev, S.S.,**
965 **Ponnala, L., Sloan, D.B., and van Wijk, K.J.** (2022). Proteomics, phylogenetics, and
966 coexpression analyses indicate novel interactions in the plastid CLP chaperone-protease
967 system. J Biol Chem **298**:101609. 10.1016/j.jbc.2022.101609.
968 **Rekhter, D., Lüdke, D., Ding, Y., Feussner, K., Zienkiewicz, K., Lipka, V., Wiermer, M.,**
969 **Zhang, Y., and Feussner, I.** (2019). Isochorismate-derived biosynthesis of the plant stress
970 hormone salicylic acid. Science **365**:498–502. 10.1126/science.aaw1720.
971 **Richter, A.S., Nagele, T., Grimm, B., Kaufmann, K., Schroda, M., Leister, D., and Kleine, T.**
972 (2023). Retrograde signaling in plants: A critical review focusing on the GUN pathway and
973 beyond. Plant Commun **4**:100511. 10.1016/j.xplc.2022.100511.
974 **Rodriguez-Concepcion, M., D'Andrea, L., and Pulido, P.** (2019). Control of plastidial
975 metabolism by the Clp protease complex. J Exp Bot **70**:2049–2058. 10.1093/jxb/ery441.
976 **Rudella, A., Friso, G., Alonso, J.M., Ecker, J.R., and van Wijk, K.J.** (2006). Downregulation
977 of ClpR2 leads to reduced accumulation of the ClpPRS protease complex and defects in
978 chloroplast biogenesis in Arabidopsis. Plant Cell **18**:1704–1721. 10.1105/tpc.106.042861.
979 **Selinski, J., Scheibe, R., Day, D.A., and Whelan, J.** (2018). Alternative Oxidase Is Positive for
980 Plant Performance. Trends Plant Sci **23**:588–597. 10.1016/j.tplants.2018.03.012.
981 **Sjogren, L.L., and Clarke, A.K.** (2011). Assembly of the chloroplast ATP-dependent Clp
982 protease in Arabidopsis is regulated by the ClpT accessory proteins. Plant Cell **23**:322–332.
983 10.1105/tpc.110.082321.
984 **Sjogren, L.L., Stanne, T.M., Zheng, B., Sutinen, S., and Clarke, A.K.** (2006). Structural and
985 functional insights into the chloroplast ATP-dependent Clp protease in Arabidopsis. Plant
986 Cell **18**:2635–2649. 10.1105/tpc.106.044594.
987 **Sun, J.L., Li, J.Y., Wang, M.J., Song, Z.T., and Liu, J.X.** (2021). Protein Quality Control in
988 Plant Organelles: Current Progress and Future Perspectives. Mol Plant **14**:95–114.
989 10.1016/j.molp.2020.10.011.
990 **Sun, Y., and Jarvis, R.P.** (2023). Chloroplast Proteostasis: Import, Sorting, Ubiquitination, and
991 Proteolysis. Annu Rev Plant Biol **74**:259–283. 10.1146/annurev-arplant-070122-032532.
992 **Susila, H., Nasim, Z., Gawarecka, K., Jung, J.Y., Jin, S., Youn, G., and Ahn, J.H.** (2023).
993 Chloroplasts prevent precocious flowering through a GOLDEN2-LIKE-B-BOX DOMAIN
994 PROTEIN module. Plant Commun **4**:100515. 10.1016/j.xplc.2023.100515.
995 **Tang, Q., Xu, D., Lenzen, B., Brachmann, A., Yapa, M.M., Doroodian, P., Schmitz-**
996 **Linneweber, C., Masuda, T., Hua, Z., Leister, D., et al.** (2024). GENOMES

997 UNCOUPLED PROTEIN1 binds to plastid RNAs and promotes their maturation. Plant
998 Commun **5**:101069. 10.1016/j.xplc.2024.101069.
999 **Tapken, W., Kim, J., Nishimura, K., van Wijk, K.J., and Pilon, M.** (2015). The Clp protease
1000 system is required for copper ion-dependent turnover of the PAA2/HMA8 copper transporter
1001 in chloroplasts. New Phytol **205**:511–517. 10.1111/nph.13093.
1002 **Thimm, O., Blasing, O., Gibon, Y., Nagel, A., Meyer, S., Kruger, P., Selbig, J., Muller, L.A.,**
1003 **Rhee, S.Y., and Stitt, M.** (2004). MAPMAN: a user-driven tool to display genomics data
1004 sets onto diagrams of metabolic pathways and other biological processes. Plant J **37**:914–939.
1005 10.1111/j.1365-313x.2004.02016.x.
1006 **Tzvetkova-Chevolleau, T., Franck, F., Alawady, A.E., Dall'Osto, L., Carriere, F., Bassi, R.,**
1007 **Grimm, B., Nussaume, L., and Havaux, M.** (2007). The light stress-induced protein ELIP2
1008 is a regulator of chlorophyll synthesis in Arabidopsis thaliana. Plant J **50**:795–809.
1009 10.1111/j.1365-313X.2007.03090.x.
1010 **van Wijk, K.J.** (2024). Intra-chloroplast proteases: A holistic network view of chloroplast
1011 proteolysis. Plant Cell **36**:3116–3130. 10.1093/plcell/koae178.
1012 **Wachsman, G., Modliszewski, J.L., Valdes, M., and Benfey, P.N.** (2017). A SIMPLE Pipeline
1013 for Mapping Point Mutations. Plant Physiol **174**:1307–1313. 10.1104/pp.17.00415.
1014 **Wang, Y., Berkowitz, O., Selinski, J., Xu, Y., Hartmann, A., and Whelan, J.** (2018). Stress
1015 responsive mitochondrial proteins in Arabidopsis thaliana. Free Radic Biol Med **122**:28–39.
1016 10.1016/j.freeradbiomed.2018.03.031.
1017 **Wang, Y., Selinski, J., Mao, C., Zhu, Y., Berkowitz, O., and Whelan, J.** (2020). Linking
1018 mitochondrial and chloroplast retrograde signalling in plants. Philos Trans R Soc Lond B Biol
1019 Sci **375**:20190410. 10.1098/rstb.2019.0410.
1020 **Waters, E.R., and Vierling, E.** (2020). Plant small heat shock proteins - evolutionary and
1021 functional diversity. New Phytol **227**:24–37. 10.1111/nph.16536.
1022 **Woodson, J.D., and Chory, J.** (2008). Coordination of gene expression between organellar and
1023 nuclear genomes. Nat Rev Genet **9**:383–395. 10.1038/nrg2348.
1024 **Wu, G.Z., Meyer, E.H., Richter, A.S., Schuster, M., Ling, Q., Schottler, M.A., Walther, D.,**
1025 **Zoschke, R., Grimm, B., Jarvis, R.P., et al.** (2019). Control of retrograde signalling by
1026 protein import and cytosolic folding stress. Nat Plants **5**:525–538. 10.1038/s41477-019-0415-
1027 y.
1028 **Xie, Y.D., Li, W., Guo, D., Dong, J., Zhang, Q., Fu, Y., Ren, D., Peng, M., and Xia, Y.** (2010).
1029 The Arabidopsis gene SIGMA FACTOR-BINDING PROTEIN 1 plays a role in the
1030 salicylate- and jasmonate-mediated defence responses. Plant Cell Environ **33**:828–839.
1031 10.1111/j.1365-3040.2009.02109.x.
1032 **Zhang, H., Zhang, L., Ji, Y., Jing, Y., Li, L., Chen, Y., Wang, R., Zhang, H., Yu, D., and**
1033 **Chen, L.** (2022). Arabidopsis SIGMA FACTOR BINDING PROTEIN1 (SIB1) and SIB2
1034 inhibit WRKY75 function in abscisic acid-mediated leaf senescence and seed germination. J
1035 Exp Bot **73**:182–196. 10.1093/jxb/erab391.

1036

1037 **FIGURE LEGENDS**

1038 **Figure 1. Identification and confirmation of *FMT* as the causal gene for suppressor**
1039 **mutations of *clpc1-1*.**

1040 **(A)** Workflow of EMS mutagenesis, suppressor screening, and bulked segregant analysis. Seeds
1041 of *clpc1-1* were mutagenized with ethyl methanesulfonate (EMS) (~10,000 seeds), and M2
1042 plants were screened for suppressor mutants exhibiting a green-leaf phenotype. Selected M2
1043 plants were backcrossed to the parental *clpc1-1* line (M0) to generate BC1F2 progeny. Pooled
1044 DNA from green BC1F2 plants was subjected to whole-genome sequencing (WGS), and
1045 mutations were identified using the SIMPLE pipeline (Wachsman et al., 2017).

1046 **(B)** Growth and development of wild-type (Col-0), *clpc1-1*, and four independent *clpc1-1*
1047 suppressor mutants - designated *socc* (suppressor of *clpc1*) - including *socc20-1 clpc1-1*, *socc20-*
1048 *4 clpc1-1*, *socc39-1 clpc1-1*, and *socc43-1 clpc1-1*, grown on soil for 23 days under a 16/8 hour
1049 light/dark cycle at 100 µmol photons m^{-2} s^{-1}. Scale bar = 2 cm.

1050 **(C)** Gene model of *FMT* (At3g52140) showing the positions of T-DNA insertions (*fmt-3*, *fmt-4*)
1051 and EMS-induced mutations identified in *socc* suppressor lines. Coding exons (black boxes),
1052 untranslated regions (open boxes), and introns (gray lines) are indicated. Mutation sites are
1053 mapped relative to the *FMT* genomic structure. The EMS-induced *socc* alleles include canonical
1054 splice-site defects and splice-region variants that disrupt *FMT* coding or splicing, while the T-
1055 DNA alleles (*fmt-3* and *fmt-4*) interrupt the gene's exon–intron structure. These mutations affect
1056 *FMT* coding or splicing and are associated with the corresponding mutant phenotypes. Detailed
1057 mutation positions, nucleotide changes, and predicted effects are provided in table S1.

1058 **(D)** Genetic complementation of four suppressor mutants (*socc clpc1-1* lines) using a genomic
1059 *FMT* transgene driven by its native promoter. Transformation of each *socc clpc1-1* mutant with
1060 *pFMT:FMT* restored the yellow, chlorotic phenotype characteristic of *clpc1-1*, confirming *FMT*

1061 as the causal gene. Plants were grown on soil for 18 days under a 16/8 hour light/dark cycle at
1062 100 µmol photons m^{-2} s^{-1}. Scale bar = 2 cm.

1063 **(E)** T-DNA insertion alleles *fmt-3* and *fmt-4* suppress the *clpc1-1* phenotype, similar to EMS-
1064 derived suppressor lines. Growth and development of wild-type, *fmt-3*, *fmt-4*, *clpc1-1*, *fmt-3*
1065 *clpc1-1*, and *fmt-4 clpc1-1* plants grown on soil for 23 days under a 16/8 hour light/dark cycle at
1066 100 µmol photons m^{-2} s^{-1}. Scale bar = 2 cm.

1067 **(F)** Photosynthetic efficiency and pigment accumulation in wild type, *fmt-3, clpc1-1*, and
1068 suppressor lines. Maximum quantum efficiency of PSII (Fv/Fm), total chlorophyll content, and
1069 total carotenoid content were measured in Col-0 (wild type), *fmt-3*, *clpc1-1*, *fmt-3 clpc1-1*, and
1070 *socc20-1 clpc1-1*. Fv/Fm measurements were performed on 22–24-day-old soil-grown plants,
1071 while pigment quantifications were conducted on 21-day-old plants, all grown under a 16/8 hour
1072 light/dark cycle at 100 µmol photons m^{-2} s^{-1}. Fv/Fm values (left), total chlorophyll (middle), and
1073 total carotenoid contents (right) are shown. Chlorophyll and carotenoid contents are expressed as
1074 micrograms per milligram fresh weight (µg/mg FW). Bars represent mean ± SD (n = 7 for
1075 Fv/Fm; n = 5 for chlorophyll and carotenoid contents). Different lowercase letters indicate
1076 groups that differ significantly, as determined by one-way ANOVA followed by Tukey's range
1077 test ($P < 0.05$).

1078 **(G)** Suppression of CRISPR/Cas9-derived *clpc1* mutant alleles (*clpc1-4* and *clpc1-5*) by *fmt-3*.
1079 Growth and development of wild-type, *clpc1-1*, *clpc1-4*, *clpc1-5*, *fmt-3*, *fmt-3 clpc1-1*, *fmt-3*
1080 *clpc1-4*, and *fmt-3 clpc1-5* plants grown on soil for 20 days under a 16/8 hour light/dark cycle at
1081 100 µmol photons m^{-2} s^{-1}. Scale bar = 2 cm.

1082 **Figure 2. Genetic Interaction of various mutants with *fmt*.**

1083 **(A)** Growth and development of *clpr2-1, fmt-3 clpr2-1,* and *fmt-4 clpr2-1* mutants. Plants were
1084 grown on soil for 22 days under a 16/8 hour light/dark cycle at 100 µmol photons m^{-2} s^{-1}. Scale
1085 bar = 1 cm.

1086 **(B)** Growth and development of *clpt1-2 clpt2-1* and *fmt-4 clpt1-2 clpt2-1* mutants. Plants were
1087 grown on soil for 29 days under the same conditions. Scale bar = 1 cm.

1088 **(C)** Growth and development of *fmt-3, ppi1-1,* and *fmt-3 ppi1-1* mutants. Plants were grown on
1089 soil for 24 days under the same conditions. Scale bar = 2 cm.

1090 **(D)** Growth and development of *fmt-3, fmt-4, tic40-4, fmt-3 tic40-4,* and *fmt-4 tic40-4* mutants.
1091 Plants were grown on soil for 20 days under the same conditions. Scale bar = 2 cm.

1092 **(E)** Growth and development of wild-type (Col-0), *fmt-3*, *fmt-4*, *socc20-1*, *gun1-101*, *fmt-3 gun1-*
1093 *101*, *fmt-4 gun1-101*, and *socc20-1 gun1-101* plants grown on soil for 21 days under a 16/8 hour
1094 light/dark cycle at 100 µmol photons m^{-2} s^{-1}. Variegated phenotypes were observed in all *fmt*
1095 *gun1-101* double mutants. Scale bar = 2 cm.

1096 **(F)** Growth and development of *clpc1-1*, *fmt-3 clpc1-1*, *fmt-4 clpc1-1*, *socc20-1 clpc1-1*, *clpc1-1*
1097 *gun1-101*, *fmt-3 clpc1-1 gun1-101*, *fmt-4 clpc1-1 gun1-101*, and *socc20-1 clpc1-1 gun1-101*
1098 plants grown on soil for 21 days under a 16/8 hour light/dark cycle at 100 µmol photons m^{-2} s^{-1}.
1099 Suppression of the *clpc1-1 gun1-101* growth defect was observed in all *fmt clpc1-1 gun1-101*
1100 triple mutants. Scale bar = 2 cm.

1101 **Figure 3. Loss of FMT restores chloroplast morphology and protease activity through**
1102 **compensatory upregulation of *CLPC2*.**

1103 **(A)** Chloroplast ultrastructure in *fmt-3clpc1-1* and *clpc1-1*. Left panel: Transmission electron
1104 microscopy (TEM) of chloroplasts from *fmt-3 clpc1-1* leaf mesophyll cells. Chloroplasts exhibit
1105 compact morphology, well-organized grana stacks, and dense stromal regions, closely
1106 resembling wild type. Notably, mitochondria remain tightly clustered, consistent with the known
1107 *fmt* phenotype. Scale bar = 1 µm.

1108 Right panel: TEM of chloroplasts from *clpc1-1*. Chloroplasts appear swollen and rounded, with
1109 fewer and less organized thylakoid membranes and smaller, loosely stacked grana. Stromal
1110 regions are less compact than in the double mutant. Scale bar = 1 µm. m, mitochondria; c,
1111 chloroplast.

1112 **(B)** Immunoblot analysis of selected chloroplast proteins in Col-0, *clpc1-1*, *fmt-4*, *fmt-4 clpc1-1*,
1113 and *socc20-1 clpc1-1*. Antibodies used: ClpF (a Clp N-recognin adaptor protein), ClpS1 (a
1114 substrate selector for the Clp complex), and PAA2 (a Clp substrate involved in thylakoid copper
1115 transport). Each lane was loaded with either 10 µg (1×) or 30 µg (3×) of total chloroplast protein.
1116 Coomassie Brilliant Blue (CBB) staining shows equal loading.

1117 **(C)** PAA2 degradation assay using total protein extracts treated with or without $CuSO_4$. In Col-0,
1118 Cu^{2+} exposure leads to decreased PAA2 levels, whereas in *clpc1-1*, PAA2 remains elevated
1119 regardless of treatment. Cu^{2+}-dependent degradation is restored in *fmt-3 clpc1-1*, *fmt-4 clpc1-1*,
1120 and *socc20-1 clpc1-1*. No degradation is observed in *fmt-3 clpr2-1*. Ponceau S staining confirms
1121 equal loading.

1122 **(D)** Quantitative RT-PCR analysis of *CLPC2* transcript levels in wild type (Col-0), *fmt-3, fmt-4*,
1123 *fmt-3 clpc1-1, fmt-4 clpc1-1*, *socc20-1 clpc1-1*, *clpc1-1*, *FMT/clpc1-1* overexpression (OE) lines
1124 (#1–2), and *clpc1-1 clpc2-2*. For comparison, *CLPD* transcript levels are shown for wild type

1125 (Col-0), *fmt-3*, *fmt-3 clpc1-1*, *clpc1-1*, and *FMT/clpc1-1* OE#1. Data represent means ± SD from
1126 three biological replicates.

1127 **(E)** Growth phenotype of *clpc1-1* and independent *pCLPC2:gCLPC2/clpc1-1* overexpression
1128 (OE) lines (#1–3) grown on soil for 18 days under a 16/8 hour light/dark cycle at 90 µmol
1129 photons m^{-2} s^{-1}. Scale bar = 2 cm.

1130 **(F)** Total chlorophyll (a + b) accumulation in the lines shown in (E). Chlorophyll contents were
1131 quantified in 25-day-old plants grown under the same conditions and are expressed as
1132 micrograms per milligram fresh weight (µg/mg FW). Values represent mean ± SD (n = 5).

1133 **(G)** RT–qPCR analysis of *CLPC1* and *CLPC2* transcript levels in the same lines shown in (E).
1134 OE lines with higher *CLPC2* expression (e.g., OE #2 and OE #3) exhibit a greener phenotype
1135 compared with OE #1. Bars represent mean ± SD (n = 3).

1136 **(H)** Growth and development of *clpc1-1*, *clpc1-1 clpc2-2*, and *FMT/clpc1-1* plants grown on soil
1137 for 17 days under a 16/8 hour light/dark cycle at 100 µmol photons m^{-2} s^{-1}. Both *clpc1-1 clpc2-2*
1138 and *FMT/clpc1-1* plants exhibited severely stunted and chlorotic phenotypes compared to *clpc1-*
1139 *1*. Overexpression lines were slightly larger than *clpc1-1 clpc2-2*.

1140 **(I)** Photosynthetic efficiency and total chlorophyll (a + b) accumulation in the same lines shown
1141 in (H). Maximum quantum efficiency of PSII (Fv/Fm; upper) and total chlorophyll contents
1142 (lower) were measured in 24-day-old soil-grown plants grown under a 16/8 hour light/dark cycle
1143 at 100 µmol photons m^{-2} s^{-1}. Chlorophyll contents are expressed as micrograms per milligram
1144 fresh weight (µg/mg FW). Bars represent mean ± SD (n = 15 for Fv/Fm; n = 5 for chlorophyll
1145 contents). (D), (F), (G) and (I) Different lowercase letters indicate groups that differ
1146 significantly, as determined by one-way ANOVA followed by Tukey's range test ($P < 0.05$).

1147

1148 **Figure 4. RNA expression patterns across the five genotypes wild type (Col-0), *fmt, clpc1,***
1149 ***fmtclpc1* and *FMT/clpc1*.**

1150 **(A)** Principal Component Analysis (PCA) of RNA-seq data showing clustering of biological
1151 replicates by genotype.

1152 **(B)** Hierarchical cluster analysis of z-score-normalized average RNA abundance of 4745 protein-
1153 coding nuclear genes in WT*, fmt, clpc1, fmtclpc1* and *FMT/clpc1* sampled at stage 1.07. Only
1154 genes that show at least one pairwise significance difference (adj P<0.01 and at least 2-fold
1155 difference) between 2 genotypes are included. The cladogram has three main clusters (I, II, III)
1156 with three subclusters each. The scaling of heat map is shown in the top right. The z-score was
1157 calculated as (individual value-average)/standard deviation for each gene across the 5 genotypes.

1158 **(C)** MapMan functional bin distribution across clusters I, II and III for all genes in the cladogram
1159 (4745 genes). Only bins with more than 10 genes are shown.

1160 **(D)** MapMan functional bin distribution of plastid and mitochondrial proteins across clusters I, II
1161 and III (638 genes). Only bins with more than 10 genes are shown.

1162 **(E)** Differential expression of the transcription factors **HSFA2, GLK1, BBX15, and WRKY40**.
1163 RNA-seq–normalized counts are shown as means ± SD for each genotype. Statistical
1164 significance was assessed using ordinary one-way ANOVA with Tukey's multiple-comparison
1165 test. Significant differences are indicated by asterisks (**P* < 0.05, ***P* < 0.01, ****P* < 0.001,
1166 *****P* < 0.0001). Gene cluster membership is indicated.

1167 **Figure 5. Comparative analysis of total rosette proteomes of *clpc1* and *fmtclpc1* soil- grown**
1168 **seedlings in growth stage 1.07 based on NadjSPC.**

1169 **(A)** Bar diagram displaying the relative abundance of the chloroplast ClpPRT complex and
1170 ClpC2 in *fmtclpc1* and *clpc1*.

1171 **(B)** Volcano plot of the *fmtclpc1/clpc1* relative protein abundance ratio and significance of
1172 differential accumulation. Horizontal dashed lines indicate the -log10 p-value at 0.01 and the
1173 vertical dashed lines indicate 2-fold protein abundance difference between *fmtclpc1* and *clpc1*.

1174 **(C)** Bar diagram displaying the relative abundance of FMT and the related REC1,2,3 proteins in
1175 *fmtclpc1* and *clpc1*. *P<0.05; **P<0.01.

1176 **(D)** Bar diagram displaying the relative abundance of each of the seven HSP90 proteins in
1177 *fmtclpc1* and *clpc1*. *P<0.05; **P<0.01. HSP90-1,2,3,4 are localized to the cytosol. HSP90-5,6
1178 and 7 are respectively localized to the chloroplast (p), mitochondria (m) and endoplasmic
1179 reticulum (ER).

1180 **Figure 6. *REC1* and *REC2* are required for full suppression of *clpc1-1* by *fmt*.**

1181 **(A)** Quantitative RT-PCR analysis of *REC1*, *REC2*, and *REC3* transcript levels in wild type (Col-
1182 0), *fmt-3*, *fmt-3 clpc1-1*, *clpc1-1*, and *FMT/clpc1-1* OE#1. Data represent mean ± SD from three
1183 biological replicates.

1184 **(B)** Growth and development of wild type, *clpc1-1*, *rec1-3*, *rec2-1*, *rec3-1*, *rec1-3 clpc1-1*, *rec2-1*
1185 *clpc1-1*, and *rec3-1 clpc1-1* mutants. Plants were grown on soil for 17 days under a 16/8 hour
1186 light/dark cycle at 100 µmol photons m^{-2} s^{-1}. Scale bar = 2 cm.

1187 **(C)** Growth and development of *fmt-3 rec1-3 clpc1-1*, *fmt-3 rec2-1 clpc1-1*, *fmt-3 rec3-1 clpc1-1*,
1188 *fmt-3 clpc1-1*, and *clpc1-1* mutants. Plants were grown on soil for 18 days under a 16/8 hour
1189 light/dark cycle at 100 µmol photons m^{-2} s^{-1}. Scale bar = 2 cm.

1190 **(D)** Pigment accumulation in the same lines shown in (C). Total chlorophyll and carotenoid
1191 contents were measured in 21-day-old plants grown under a 16/8 hour light/dark cycle at 100
1192 µmol photons m^{-2} s^{-1}. Total chlorophyll (left) and total carotenoids (right) are shown. Pigment
1193 contents are expressed as micrograms per milligram fresh weight (µg/mg FW). Values represent
1194 mean ± SD (n = 5).

1195 **(E)** Quantitative RT-PCR analysis of *CLPC2* transcript levels were measured in *clpc1-1*, *fmt-3*
1196 *clpc1-1*, *fmt-3 rec1-3 clpc1-1*, *fmt-3 rec2-1 clpc1-1*, and *fmt-3 rec3-1 clpc1-1*. Data represent
1197 mean ± SD from three biological replicates. (A), (D), and (E) Different lowercase letters indicate
1198 groups that differ significantly, as determined by one-way ANOVA followed by Tukey's range
1199 test ($P < 0.05$).

1200 **(F) *clpc1*-associated plastid stress state.** Working model illustrating the transcriptional and
1201 physiological state of *clpc1* relative to wild type. Loss of ClpC1 causes chloroplast dysfunction,
1202 triggering plastid-to-nucleus retrograde signaling associated with a broadly repressive nuclear
1203 response. This state correlates with reduced expression of multiple transcription factors,

including GLK1 and BBX15, as well as decreased expression of photosynthesis-related genes. In parallel, plastid-localized metabolic response genes such as *ACC2* are upregulated, reflecting altered plastid metabolic states associated with impaired chloroplast proteostasis and the small, virescent *clpc1* phenotype. Dashed arrows denote inferred signaling relationships based on transcriptomic and phenotypic analyses.

(G) FMT-mediated recovery state in *fmtclpc1*. Working Model illustrating the transcriptional and physiological state associated with FMT-dependent suppression of *clpc1*. Loss of *FMT*, a mitochondria-associated member of the FMT–REC gene family, is associated with mitochondrial perturbation that engages a mitochondria-to-nucleus communication route. This nuclear response correlates with increased expression of *REC2* and *CLPC2*, the latter encoding a plastid Clp chaperone that compensates for loss of ClpC1 and promotes restoration of chloroplast proteostasis in *fmtclpc1*. In this recovery state, transcription factors (TFs) associated with chloroplast gene programs (GLK1, BBX15) are upregulated, photosynthesis-related genes are reactivated, and plastid stress markers such as *ACC2* and *ELIP2* are reduced. Upregulation of mitochondrial redox- and metabolism-associated factors (e.g., SLP1, SLP2, ATM3, GLDH, LPD1) is consistent with mitochondria-derived signaling. Increased expression of salicylic acid (SA)- and jasmonic acid (JA)-associated signaling components further reflects a remodeled nuclear transcriptional state. The *fmt–clpc1* interaction occurs independently of GUN1, which is depicted separately. Genes shown in red are upregulated and those in blue are downregulated based on integrated transcriptomic and proteomic datasets; dashed arrows denote inferred signaling or transcriptional relationships supported by genetic, transcriptomic, and proteomic evidence.

Fig. 1A-G

A

clpc1-1

↓

EMS mutagenesis (~10,000 M1 seeds)

↓

M2: Screen for suppressor mutants (green leaves)

↓

Cross: Selected M2 x *clpc1-1*

↓

BC1F2 segregating population

↓

Genomic DNA extraction from pooled BC1F2 → WGS

↓

SIMPLE Pipeline

↓

Candidate gene identification → Validation

B

C

D

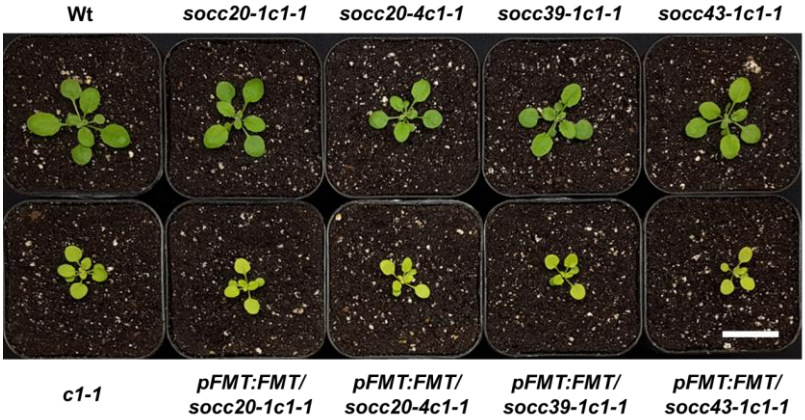

E

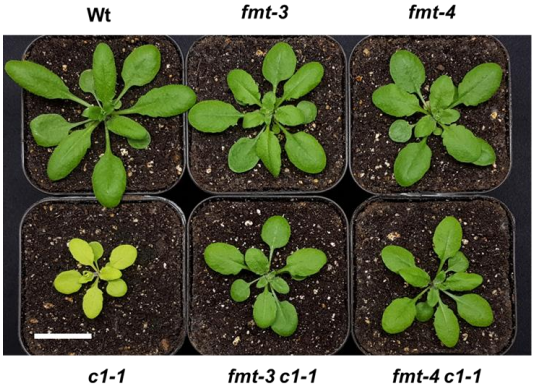

F

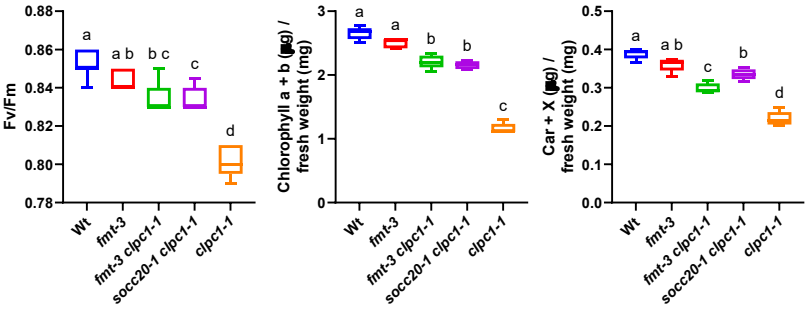

G

Fig. 2A-F

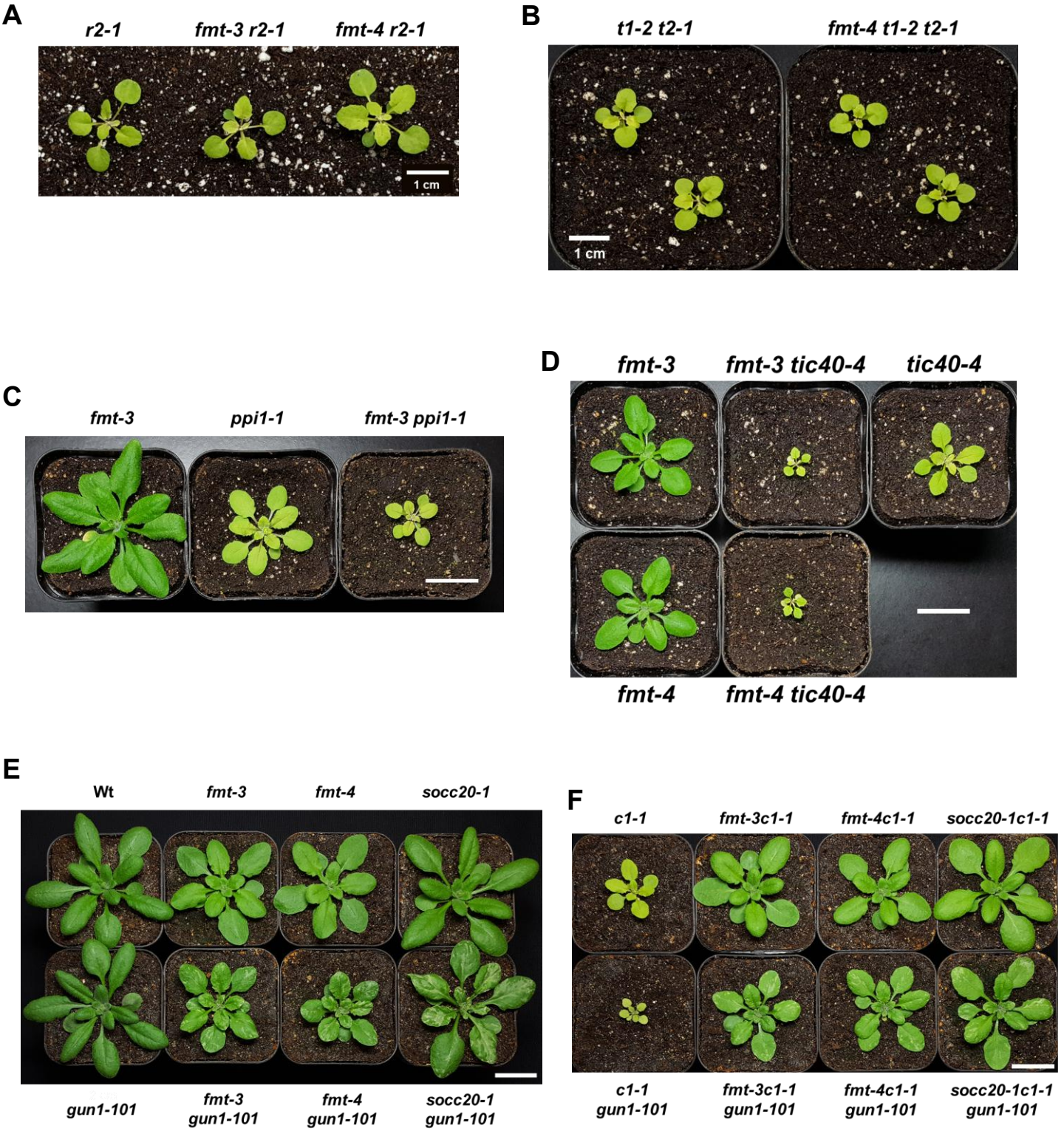
A
r2-1
fmt-3 r2-1
fmt-4 r2-1
1 cm
B
t1-2 t2-1
fmt-4 t1-2 t2-1
1 cm
C
fmt-3
ppi1-1
fmt-3 ppi1-1
D
fmt-3
fmt-3 tic40-4
tic40-4
fmt-4
fmt-4 tic40-4
E
Wt
fmt-3
fmt-4
socc20-1
gun1-101
fmt-3 gun1-101
fmt-4 gun1-101
socc20-1 gun1-101
F
c1-1
fmt-3c1-1
fmt-4c1-1
socc20-1c1-1
c1-1 gun1-101
fmt-3c1-1 gun1-101
fmt-4c1-1 gun1-101
socc20-1c1-1 gun1-101

Fig. 3A-D

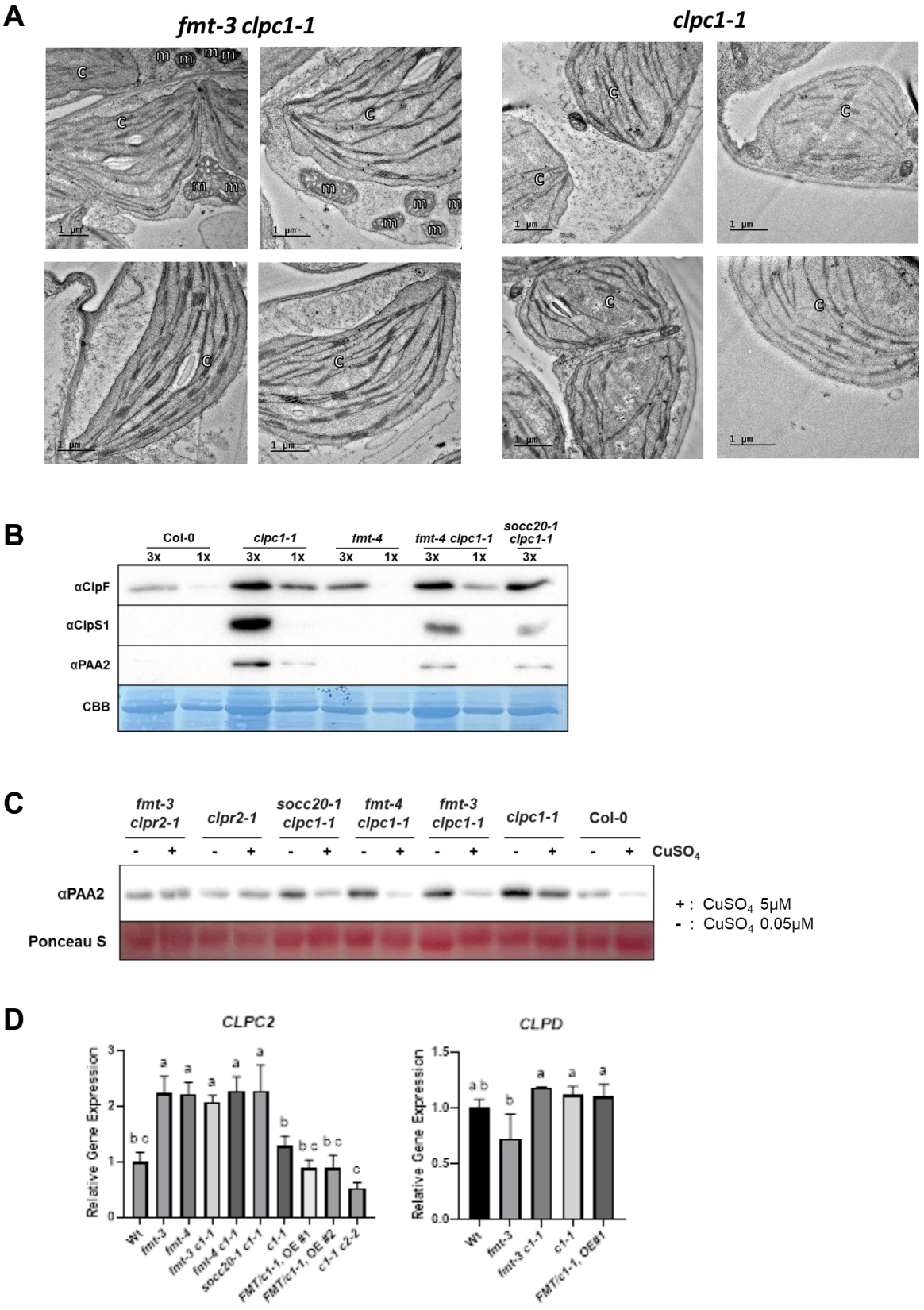
A
fmt-3 clpc1-1
clpc1-1
C
m
1 µm
B
Col-0
clpc1-1
fmt-4
fmt-4 clpc1-1
socc20-1 clpc1-1
3x
1x
αClpF
αClpS1
αPAA2
CBB
C
fmt-3 clpr2-1
clpr2-1
socc20-1 clpc1-1
fmt-4 clpc1-1
fmt-3 clpc1-1
clpc1-1
Col-0
CuSO4
αPAA2
Ponceau S
+ : CuSO4 5µM
- : CuSO4 0.05µM
D
CLPC2
CLPD
Relative Gene Expression
Wt
fmt-3
fmt-4
fmt-3 c1-1
fmt-4 c1-1
socc20-1 c1-1
c1-1
FMT/c1-1, OE #1
FMT/c1-1, OE #2
c1-1 c2-2
FMT/c1-1, OE#1

Fig. 3E-I

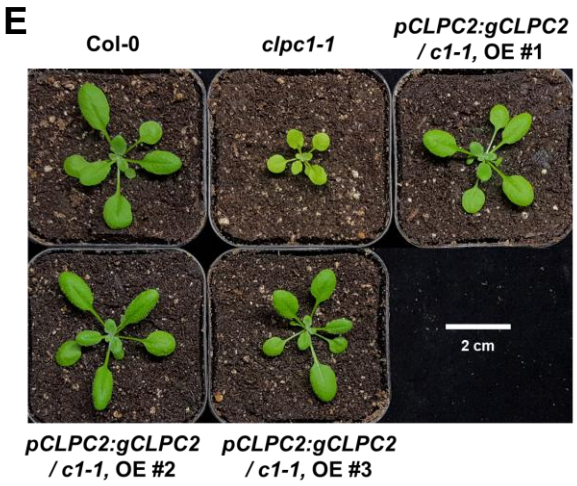
E
Col-0
clpc1-1
pCLPC2:gCLPC2 / c1-1, OE #1
2 cm
pCLPC2:gCLPC2 / c1-1, OE #2
pCLPC2:gCLPC2 / c1-1, OE #3

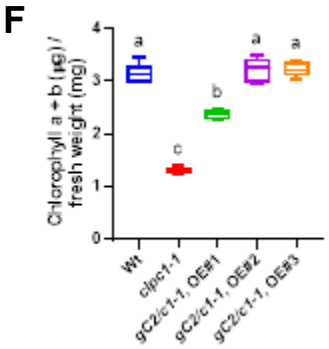
F
Chlorophyll a + b (μg) / fresh weight (mg)
Wt
clpc1-1
gC2/c1-1, OE#1
gC2/c1-1, OE#2
gC2/c1-1, OE#3

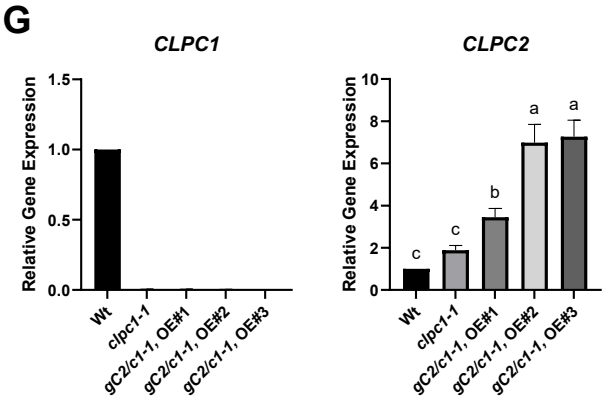
G
CLPC1
CLPC2
Relative Gene Expression
Wt
clpc1-1
gC2/c1-1, OE#1
gC2/c1-1, OE#2
gC2/c1-1, OE#3

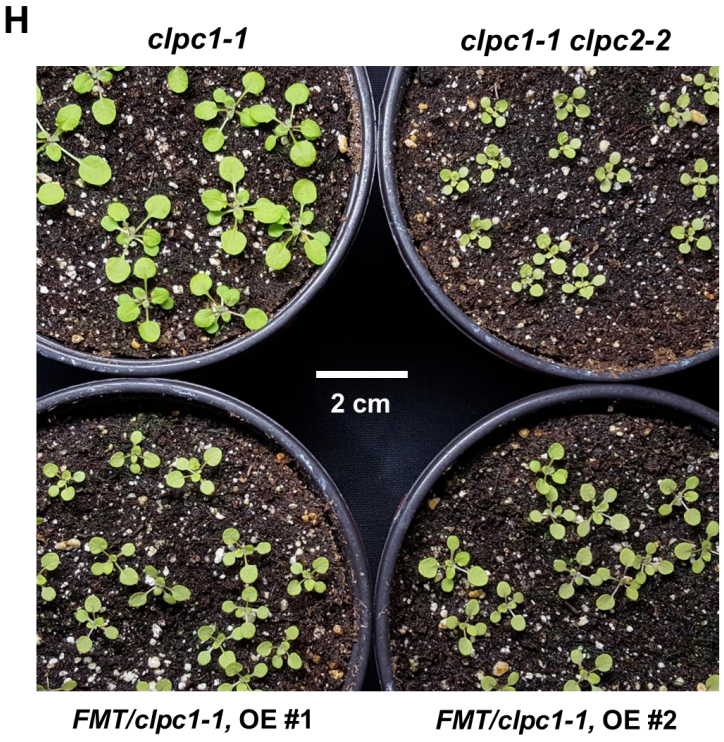
H
clpc1-1
clpc1-1 clpc2-2
2 cm
FMT/clpc1-1, OE #1
FMT/clpc1-1, OE #2

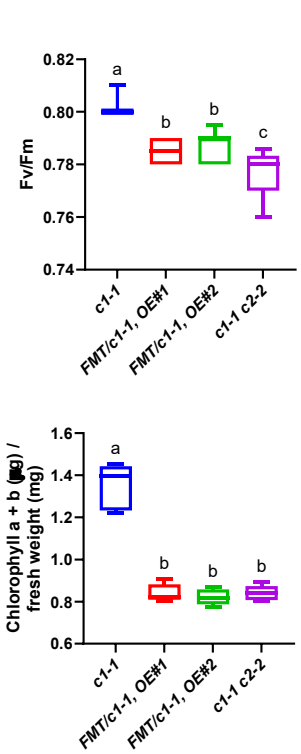
I
Fv/Fm
Chlorophyll a + b (μg) / fresh weight (mg)
c1-1
FMT/c1-1, OE#1
FMT/c1-1, OE#2
c1-1 c2-2

Fig. 4A-E

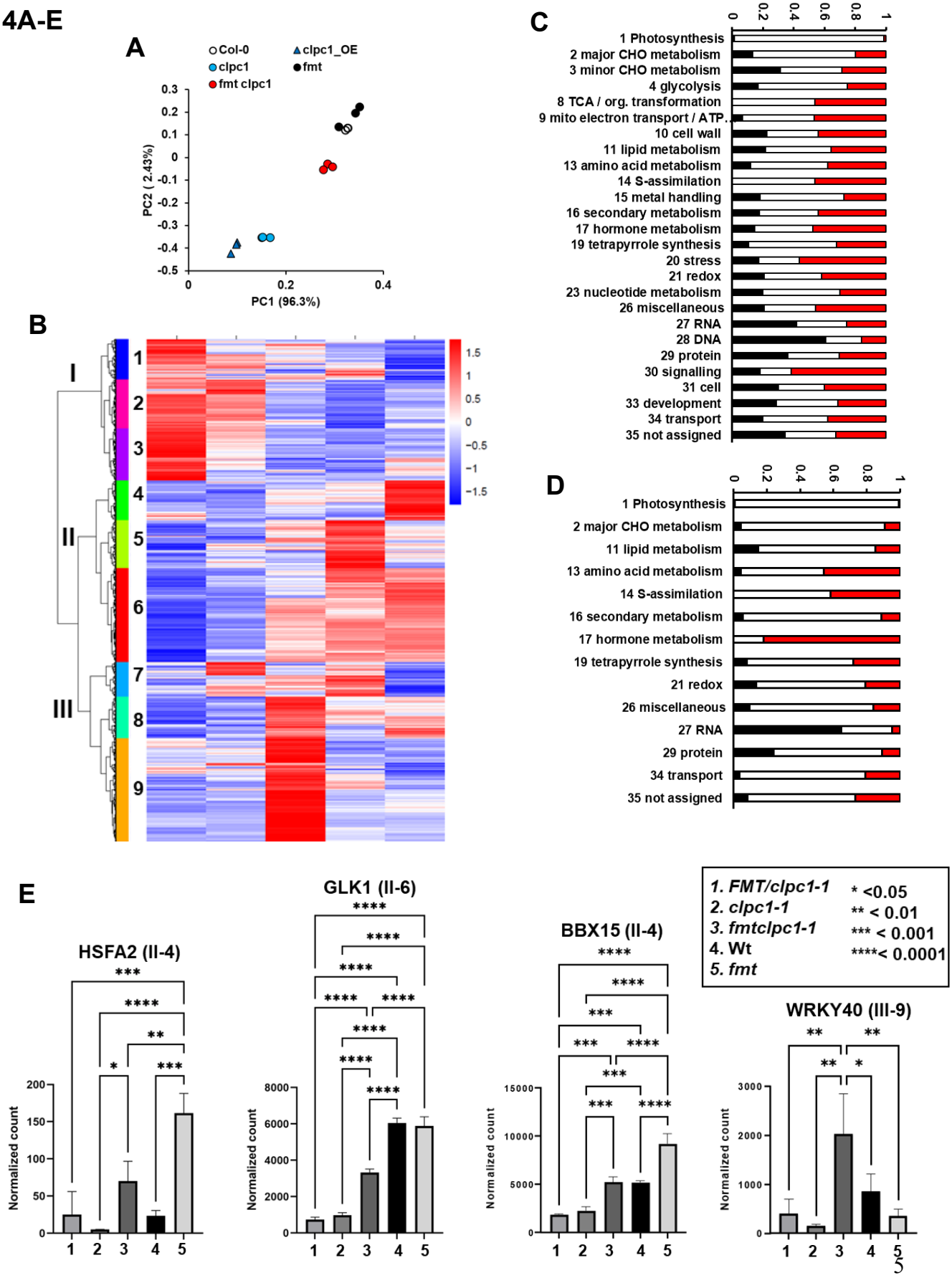
A
Col-0
clpc1
fmt clpc1
clpc1_OE
fmt
PC2 (2.43%)
PC1 (96.3%)
B
I
II
III
1
2
3
4
5
6
7
8
9
C
1 Photosynthesis
2 major CHO metabolism
3 minor CHO metabolism
4 glycolysis
8 TCA / org. transformation
9 mito electron transport / ATP..
10 cell wall
11 lipid metabolism
13 amino acid metabolism
14 S-assimilation
15 metal handling
16 secondary metabolism
17 hormone metabolism
19 tetrapyrrole synthesis
20 stress
21 redox
23 nucleotide metabolism
26 miscellaneous
27 RNA
28 DNA
29 protein
30 signalling
31 cell
33 development
34 transport
35 not assigned
D
1 Photosynthesis
2 major CHO metabolism
11 lipid metabolism
13 amino acid metabolism
14 S-assimilation
16 secondary metabolism
17 hormone metabolism
19 tetrapyrrole synthesis
21 redox
26 miscellaneous
27 RNA
29 protein
34 transport
35 not assigned
E
HSFA2 (II-4)
GLK1 (II-6)
BBX15 (II-4)
WRKY40 (III-9)
Normalized count
1. FMT/clpc1-1
2. clpc1-1
3. fmtclpc1-1
4. Wt
5. fmt
* <0.05
** < 0.01
*** < 0.001
****< 0.0001

Fig. 5A-D

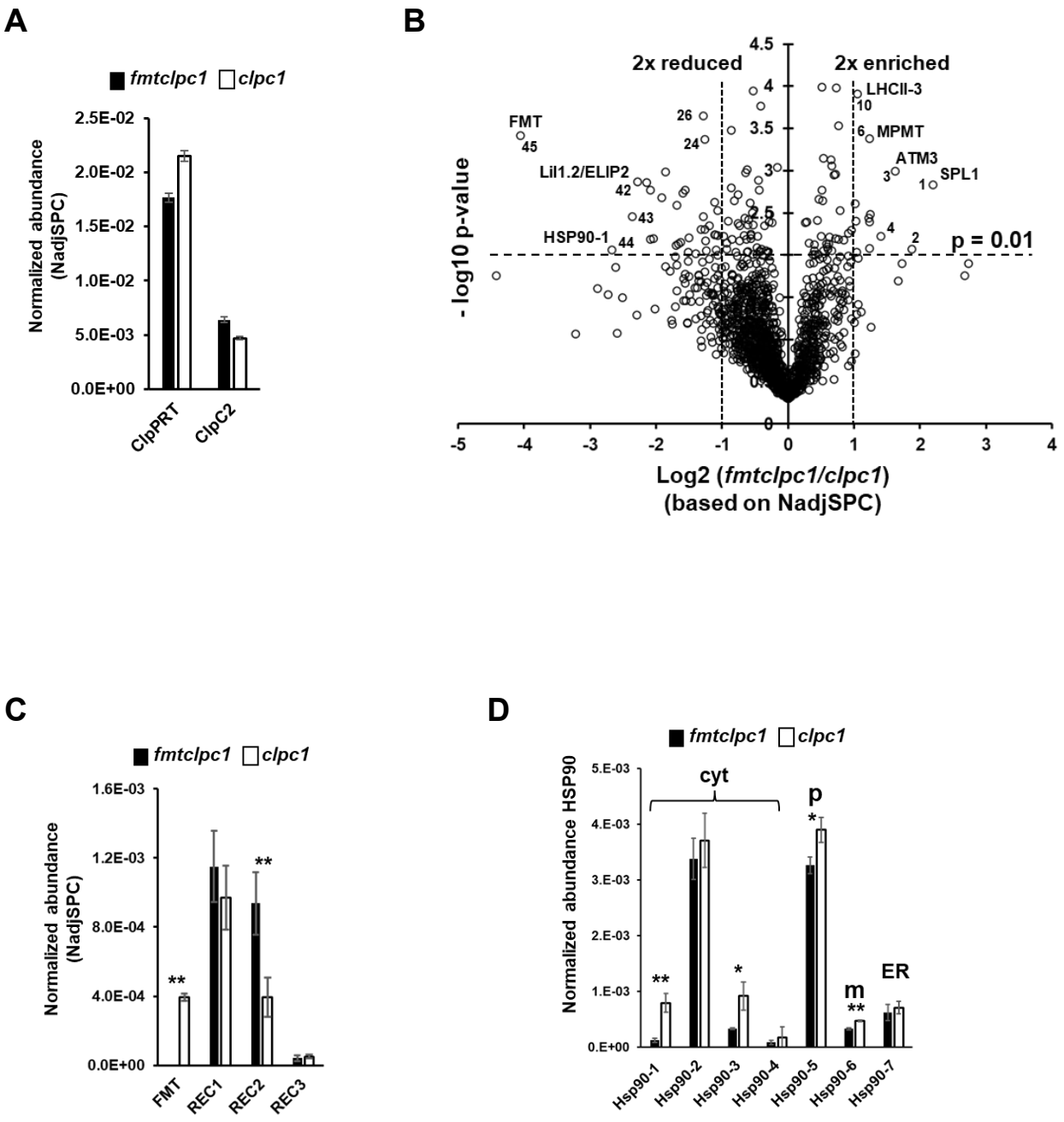
A
fmtclpc1
clpc1
Normalized abundance (NadjSPC)
2.5E-02
2.0E-02
1.5E-02
1.0E-02
5.0E-03
0.0E+00
ClpPRT
ClpC2
B
2x reduced
2x enriched
FMT
45
26
24
Lil1.2/ELIP2
42
43
HSP90-1
44
LHCII-3
10
6
MPMT
ATM3
3
SPL1
1
4
2
p = 0.01
- log10 p-value
Log2 (fmtclpc1/clpc1)
(based on NadjSPC)
C
fmtclpc1
clpc1
Normalized abundance (NadjSPC)
1.6E-03
1.2E-03
8.0E-04
4.0E-04
0.0E+00
**
**
FMT
REC1
REC2
REC3
D
fmtclpc1
clpc1
Normalized abundance HSP90
5.E-03
4.E-03
3.E-03
2.E-03
1.E-03
0.E+00
cyt
p
m
ER
**
*
*
**
Hsp90-1
Hsp90-2
Hsp90-3
Hsp90-4
Hsp90-5
Hsp90-6
Hsp90-7

Fig. 6A-E

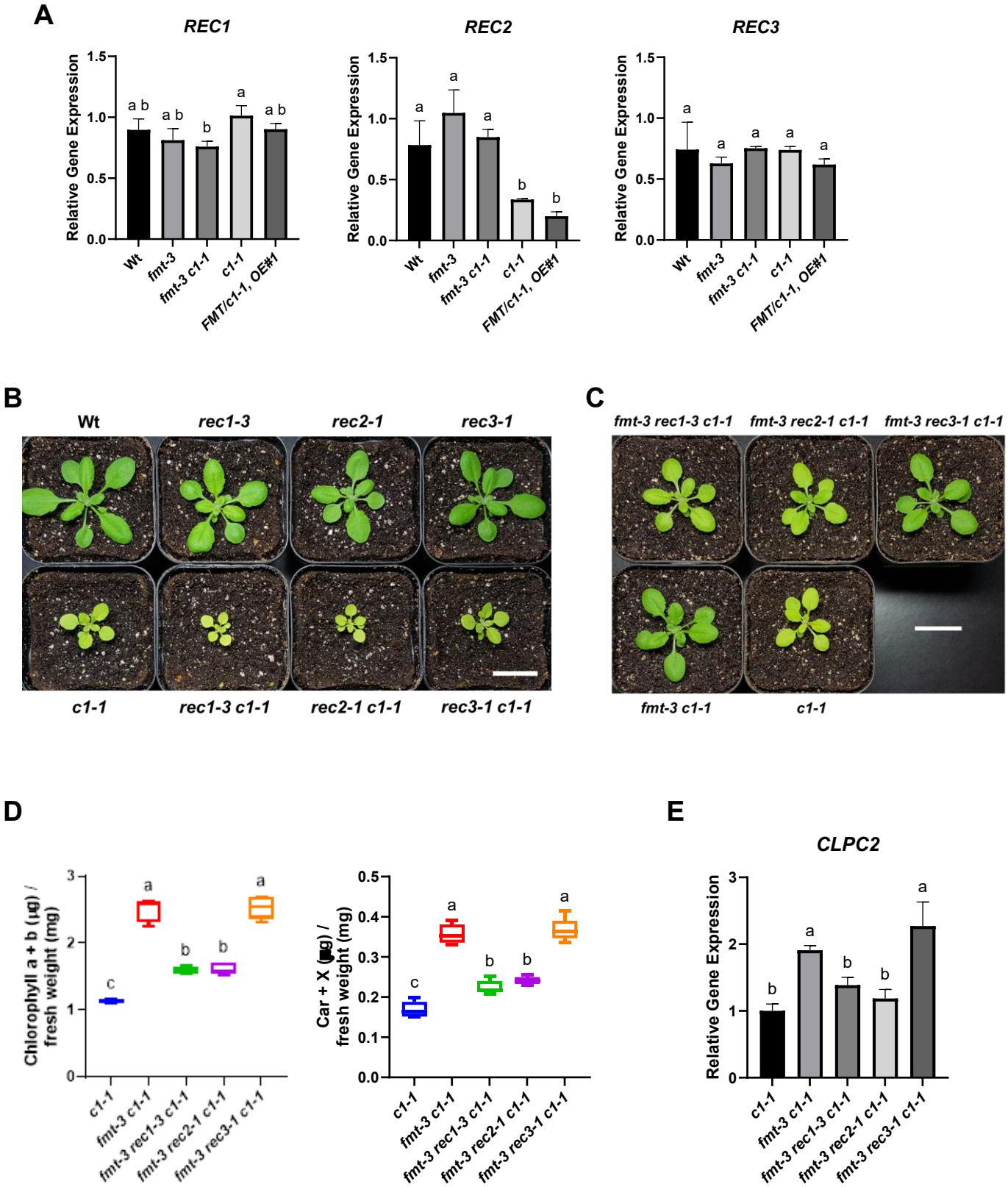
A
REC1
REC2
REC3
Relative Gene Expression
1.5
1.0
0.5
0.0
a b
a b
b
a
a b
a
a
a
b
b
a
a
a
a
a
Wt
fmt-3
fmt-3 c1-1
c1-1
FMT/c1-1, OE#1
B
Wt
rec1-3
rec2-1
rec3-1
c1-1
rec1-3 c1-1
rec2-1 c1-1
rec3-1 c1-1
C
fmt-3 rec1-3 c1-1
fmt-3 rec2-1 c1-1
fmt-3 rec3-1 c1-1
fmt-3 c1-1
c1-1
D
Chlorophyll a + b (µg) / fresh weight (mg)
3
2
1
0
c
a
b
b
a
Car + X (µg) / fresh weight (mg)
0.5
0.4
0.3
0.2
0.1
0.0
c
a
b
b
a
c1-1
fmt-3 c1-1
fmt-3 rec1-3 c1-1
fmt-3 rec2-1 c1-1
fmt-3 rec3-1 c1-1
E
CLPC2
Relative Gene Expression
3
2
1
0
b
a
b
b
a

Fig. 6F-G

F

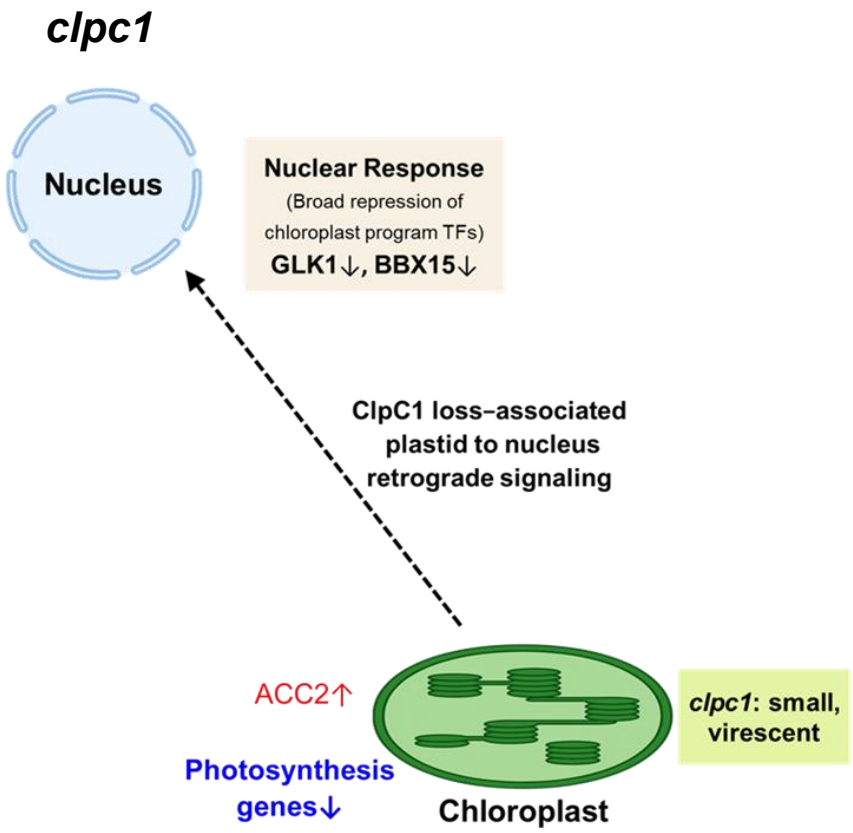
clpc1
Nucleus
Nuclear Response
(Broad repression of chloroplast program TFs)
GLK1↓, BBX15↓
ClpC1 loss-associated plastid to nucleus retrograde signaling
ACC2↑
Photosynthesis genes↓
Chloroplast
clpc1: small, virescent

G

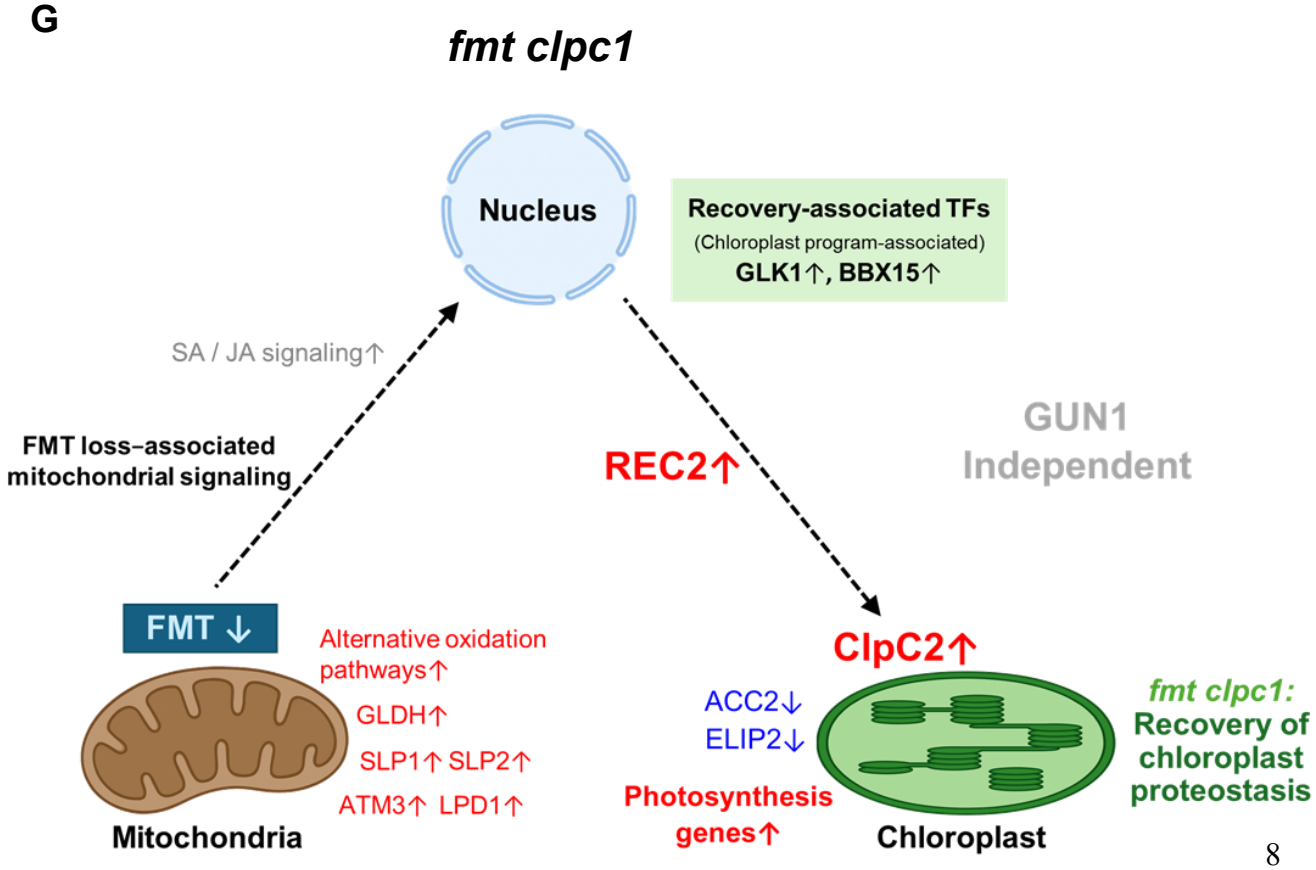
fmt clpc1
Nucleus
Recovery-associated TFs
(Chloroplast program-associated)
GLK1↑, BBX15↑
SA / JA signaling↑
FMT loss-associated mitochondrial signaling
REC2↑
GUN1 Independent
FMT ↓
Alternative oxidation pathways↑
GLDH↑
SLP1↑ SLP2↑
ATM3↑ LPD1↑
Mitochondria
ClpC2↑
ACC2↓
ELIP2↓
Photosynthesis genes↑
Chloroplast
fmt clpc1:
Recovery of chloroplast proteostasis

Table 1. Differentially accumulating proteins (p<0.01; x<0.5 or x>2) based on NadjSPC in *clpc1* vs *fmtclpc1*

Accession	#	Name	Location (a)	*fmtclpc1/clpc1* (b)	p value
AT4G27585.1	1	Stomatin-like 1 (SPL1)	m	4.587	0.001
ATCG01100.1	2	NDH A (NDH-1)	p-t	3.679	0.009
AT5G58270.1	3	ATM3 transporter of GSSG	m	3.085	0.001
AT5G47110.1	4	Lil3.1	p-t	2.654	0.006
AT3G47930.1	5	galactono-1,4-lactone dehydrogenase (GLDH)	m	2.373	0.003
AT4G25080.1	6	magnesium-protoporphyrin IX methyltransferase	p-t	2.351	0.000
AT1G44575.1	7	psbS (NPQ4 - null mutant)	p-t	2.344	0.004
AT4G28080.1	8	reduced chloroplast coverage 2 (REC2)	cyt	2.342	0.008
AT1G77090.1	9	OEC23-like-5 (TL29.8)	p-t	2.324	0.004
AT5G54270.1	10	LHCII-3	p-t	2.064	0.000
AT2G42220.1	11	rhodanese-like domain protein	p-t	2.056	0.009
AT3G08940.2	12	LHCII-4.2 - CP29	p-t	2.033	0.004
AT1G48030.1	13	E3-1 dihydrolipoamide dehydrogenase 1 (MTLPD1)	m	2.025	0.002
AT4G31120.1	14	protein arginine methyltransferase (PRMT5)	n/cyt	0.478	0.006
AT1G63680.1	15	MurE ligase family (TAC)	p	0.475	0.003
AT4G33030.1	16	UDP-sulfoquinovose synthase (SQD1)	p	0.471	0.009
AT1G53210.1	17	sodium/calcium exchanger protein	vac	0.467	0.006
AT1G12770.1	18	DExD box RNA helicase (RH47) (EMB1586)	p	0.462	0.002
AT1G47260.1	19	Carbonic anhydrase - complex I	m	0.461	0.006
AT3G61220.1	20	NADPH short-chain dehydrogenase/reductase (SDR)	cyt	0.438	0.004
AT2G22170.1	21	PLAT2- lipid-associated protein	er/cyt	0.424	0.009
AT5G06600.1	22	ubiquitin-specific protease 12 (UBP12)	n/cyt	0.418	0.007
AT3G14310.1	23	pectine methylesterase	cw	0.418	0.005
AT5G18570.1	24	GTPase Obg A2 (OBG-A2)	p	0.415	0.000
AT1G74850.1	25	pentatricopeptide (PPR) repeat (pTAC2)	p	0.410	0.000
AT1G77590.1	26	acyl-CoA synthetase (LACS9)	p	0.410	0.003
AT3G06430.1	27	PPR2- PPR protein - interacts with 23S RNA	p	0.399	0.005
AT5G37600.1	28	glutamine synthetase (GS1)	cyt	0.352	0.006
AT3G61260.1	29	remorin protein	pm	0.349	0.009
AT5G65720.1	30	NFS1 or AtMtNIFS	m	0.338	0.002
AT5G05200.1	31	ABC1 kinase 9 (ABC1K9)	p	0.330	0.002
AT4G39540.1	32	shikimate kinase	p (likely)	0.324	0.007
AT1G04850.1	33	ubiquitin-associated (UBA)	not plastid	0.316	0.007
AT3G28290.1	34	integrin-related protein 14a	pm/cyt	0.311	0.003
AT2G20020.1	35	CAF1 - splice factor group II intron	p	0.308	0.008
AT1G78510.1	36	solanesyl diphosphate synthase 1 (SPS1) - PQ9/PC8 synthesi	p	0.276	0.001
AT3G22120.1	37	Cell wall plasma membrane linker protein (CWLP)	cw	0.266	0.002
AT2G32520.1	38	dienelactone hydrolase	not plastid	0.242	0.006
AT2G26900.1	39	pyruvate importer (BASS2)	p	0.236	0.002
AT2G29530.1	40	Translocase inner membrane subunit 10 (TIM10)	m	0.235	0.007
AT3G02060.1	41	DEAD/DEAH box helicase	p	0.226	0.001
AT1G30120.1	42	Plastidial Pyruvate Dehydrogenase E1 -beta subunit	p	0.205	0.001
AT4G14690.1	43	Lil1.2 - Elip2	p-t	0.194	0.004
AT5G52640.1	44	HSP90-1 (HSP81/83)	cyt	0.157	0.009
AT3G52140.1	45	FRIENDLY (related to REC1,2,3)	cyt	0.060	0.000

(a) p = plastid, p-t = plastid-thylakoid, m = mitochondria, cyt = cytosol, vac = vacuole, pm = plasma membrane, er = endoplasmic retinulum, n = nucleus, cw = cell wall
(b) relative abundance ratio for fmtclpc1/clpc1 based on NadjSPC

Supplemental Figures

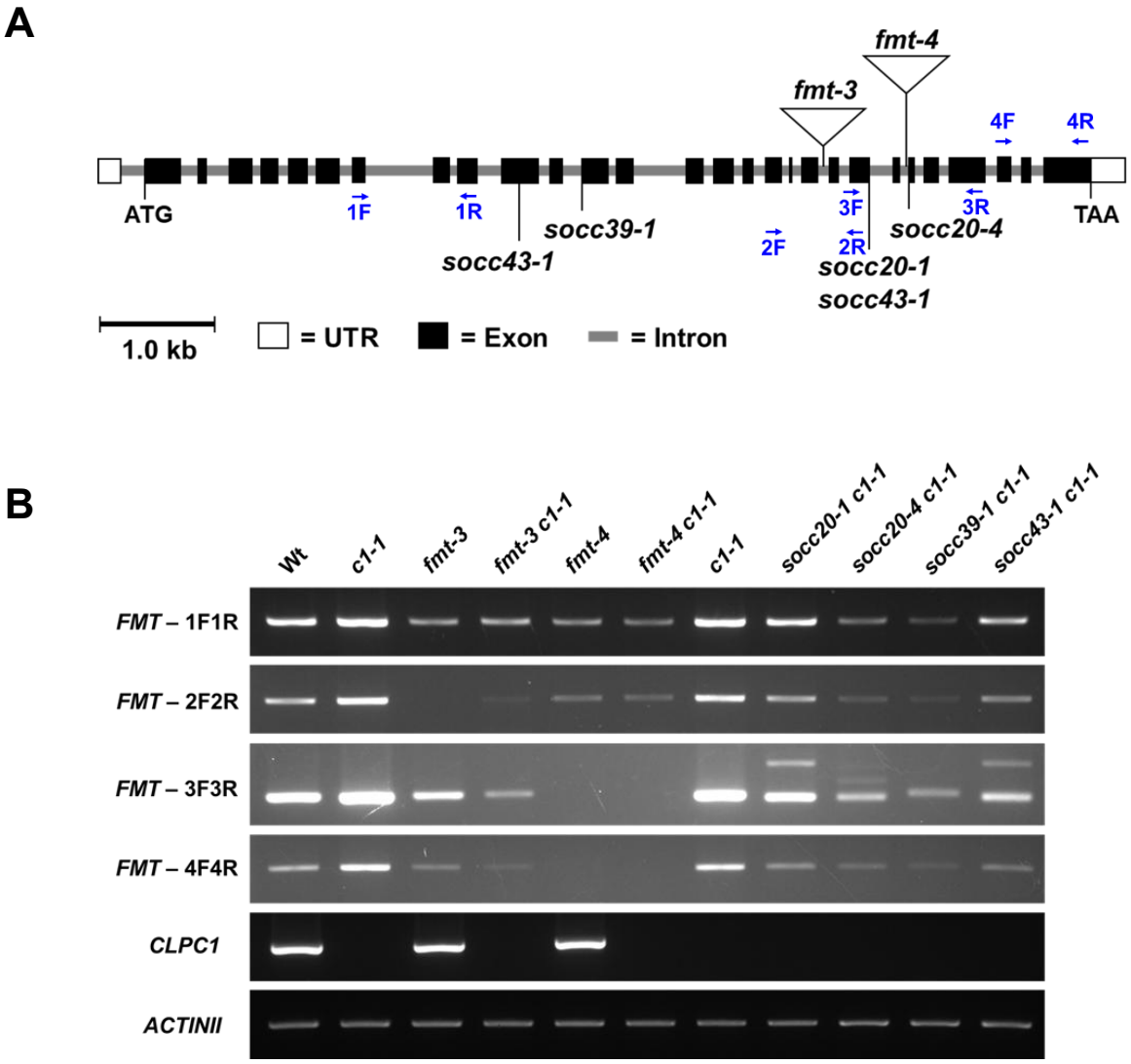

Supplemental Figure 1. Analysis of *FMT* and *CLPC1* transcript accumulation by semi-quantitative RT-PCR. (A) *FMT* (At3g52140) gene model illustrating the positions of RT-PCR primer sets used in this study: *FMT*-1F1R (exons 7–9), *FMT*-2F2R (exons 17–21), *FMT*-3F3R (exons 21–25), and *FMT*-4F4R (exons 26–28). **(B)** Semi-quantitative RT-PCR analysis of *FMT* and *CLPC1* transcript levels in Col-0, *clpc1-1*, *fmt-3*, *fmt-3 clpc1-1*, *fmt-4*, *fmt-4 clpc1-1*, *socc20-1 clpc1-1*, *socc20-4 clpc1-1*, *socc39-1 clpc1-1*, and *socc43-1 clpc1-1*. *ACTINII* was used as a control. *ACTINII* was amplified for 22 cycles, while all other targets were amplified for 25 cycles. *FMT* expression was reduced in all *fmt* alleles, with complete loss in *fmt-4*, while *CLPC1* transcripts were absent in all *clpc1-1* backgrounds.

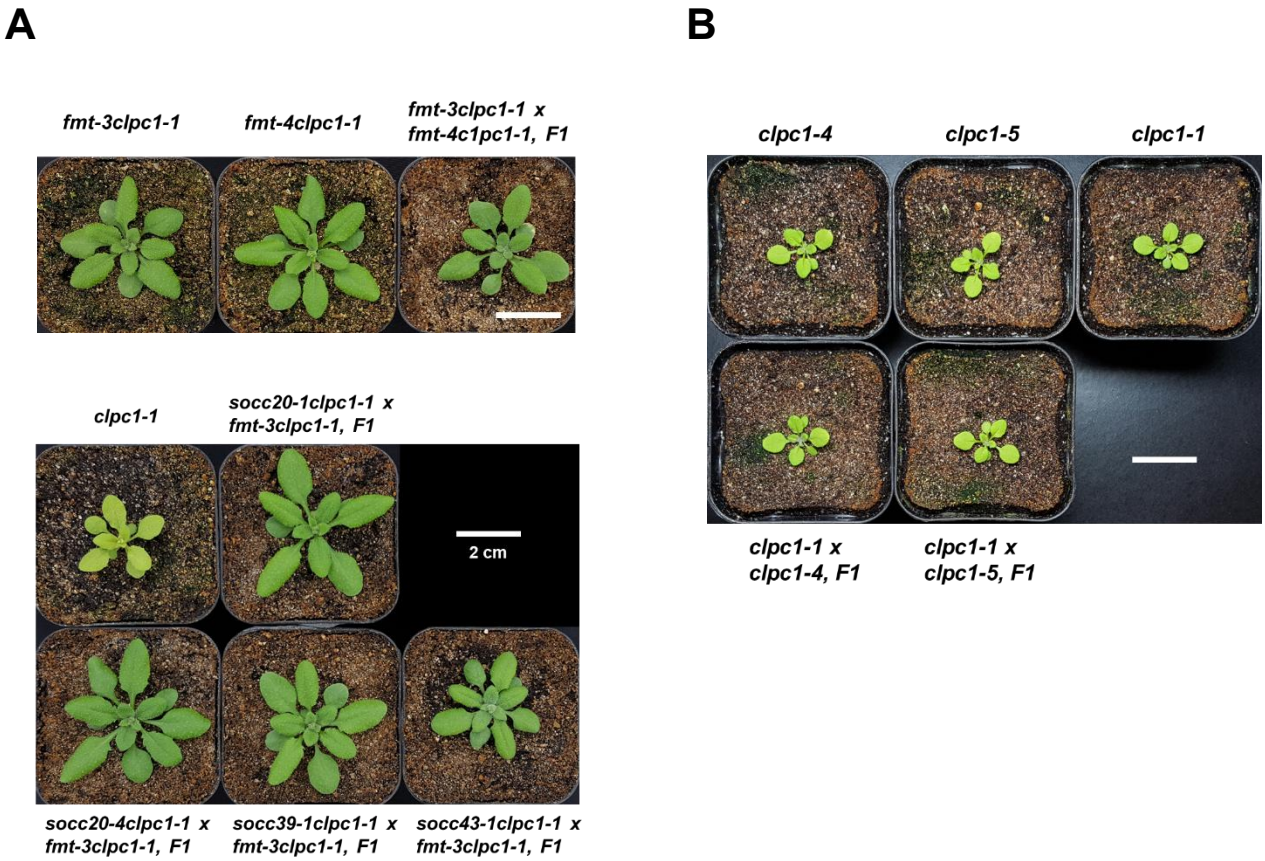

Supplemental Figure 2. Heteroallelic analysis confirms that EMS-derived suppressors and CRISPR alleles affect *FMT* and *CLPC1*, respectively. (A) Heteroallelic crosses demonstrate that EMS-derived suppressors are allelic to *FMT*. Top panel: Growth and development of *fmt-3 clpc1-1*, *fmt-4 clpc1-1*, and F1 progeny from the *fmt-3 clpc1-1* × *fmt-4 clpc1-1* cross. Plants were grown on soil for 22 days under long-day conditions (16/8 hour light/dark cycle at 100 µmol photons m^{-2} s^{-1}). Scale bar = 2 cm. Bottom panel: Growth and development of *clpc1-1* and F1 progeny from heteroallelic crosses between *fmt-3 clpc1-1* and each EMS-derived suppressor: *socc20-1 clpc1-1*, *socc20-4 clpc1-1*, *socc39-1 clpc1-1*, and *socc43-1 clpc1-1*. Plants were grown under identical conditions. Scale bar = 2 cm. **(B)** CRISPR/Cas9-derived *clpc1* alleles phenocopy *clpc1-1* in homozygous and heteroallelic combinations. Growth and development of *clpc1-1*, *clpc1-4*, *clpc1-5*, and heteroallelic F1 plants from *clpc1-1* × *clpc1-4* and *clpc1-1* × *clpc1-5* crosses. All plants were grown on soil for 16 days under long-day conditions (16/8 hour light/dark cycle at 100 µmol photons m^{-2} s^{-1}). Scale bar = 2 cm.

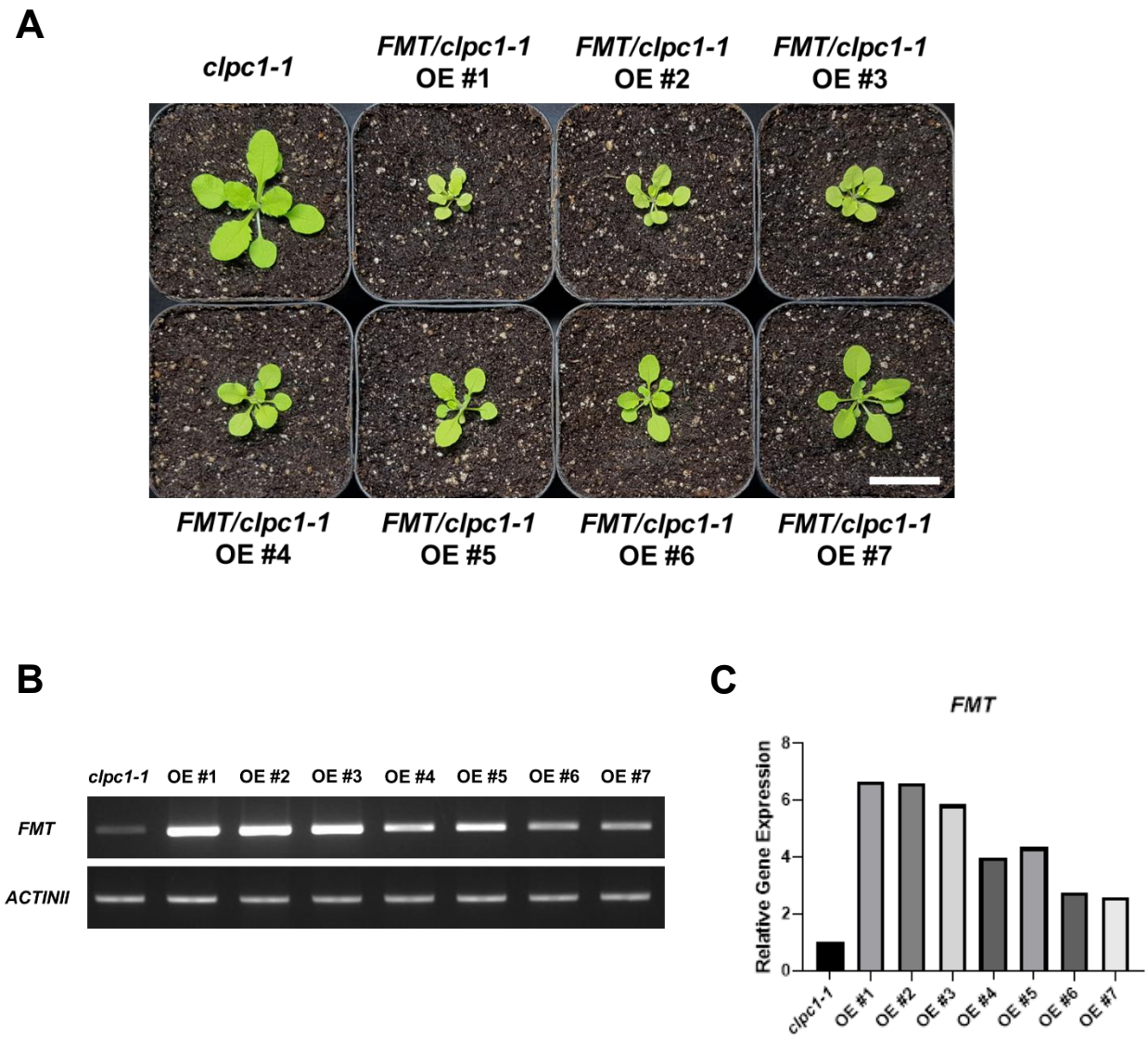

Supplemental Figure 3. Overexpression of *FMT* in *clpc1-1* results in smaller, chlorotic plants that scale with transcript abundance. (A) Growth phenotype of *clpc1-1* and independent *FMT/clpc1-1* overexpression (OE) lines (#1–7) grown on soil for 21 days under a 16/8 hour light/dark cycle at 100 µmol photons m^{-2} s^{-1}. Lines with stronger *FMT* expression exhibit smaller rosettes and more pronounced chlorosis (e.g., OE #1 shows stronger yellowing compared to OE #7). **(B)** Semi-quantitative RT-PCR analysis of *FMT* transcript levels in the same lines shown in (A). Primers targeting *FMT-RT3* (exons 21–25) were used to detect *FMT* transcript abundance. *ACTINII* served as loading control and was amplified for 22 cycles, whereas *FMT* was amplified for 25 cycles. **(C)** Quantification of *FMT* transcript abundance from (B). Both reduced plant size and chlorosis correlate negatively with *FMT* transcript levels across independent OE lines.

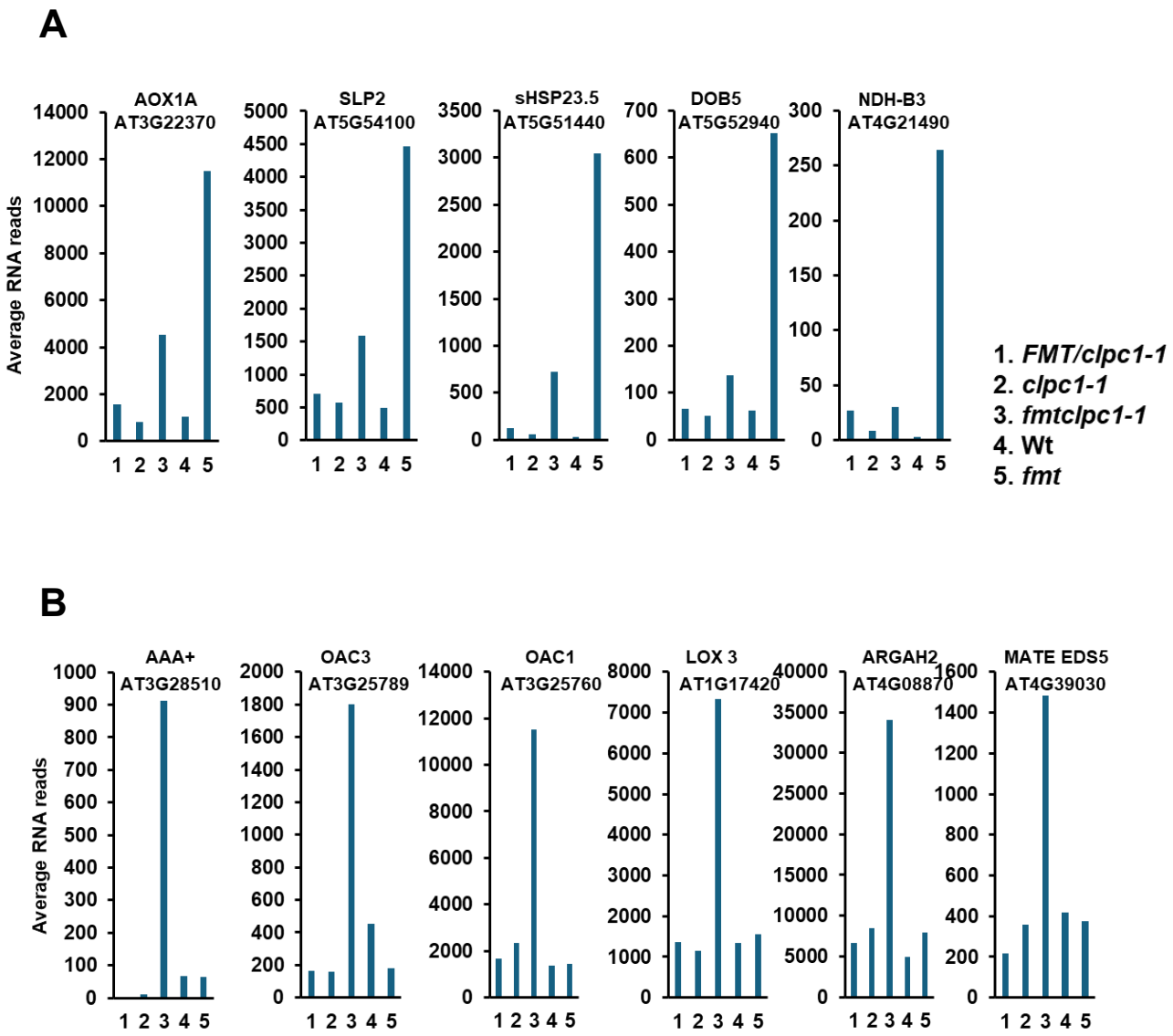

Supplemental Figure 4. RNA expression patterns of selected genes in subclusters 4, 8, and 9 across five genotypes. RNA expression levels are shown for *clpc1-1*, *FMT/clpc1-1*, *fmtclpc1-1*, *fmt*, and WT. **(A, B)** Representative genes from subcluster 4 (within cluster II) and subclusters 8 and 9 (within cluster III) exhibiting high mRNA abundance in *fmt* (subcluster 4) or *fmtclpc1* (subclusters 8 and 9) relative to the other four genotypes. **(A)** Five genes in subcluster 4 for which RNA levels in *fmt* were >3-fold higher than in each of the other genotypes. **(B)** Six genes in subclusters 8 and 9 for which RNA levels in *fmtclpc1* were >3-fold higher than in each of the other genotypes.

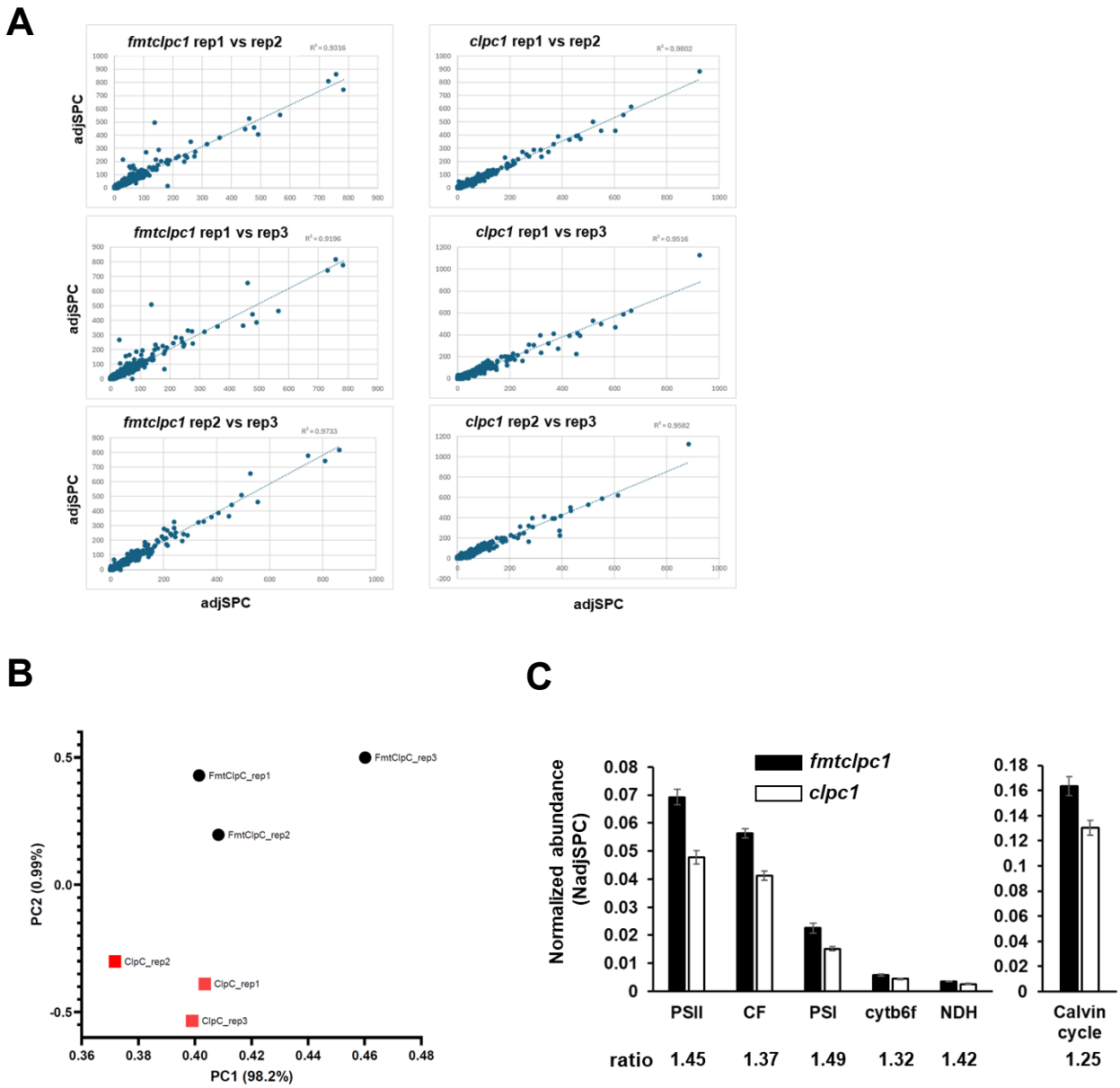

Supplemental Figure 5. Reproducibility of biological proteomics replicates and protein investments in the photosynthetic apparatus. (**A**) Cross-correlation between biological replicates for each genotype based on AdjSPC (no normalization). For clarity, the X- and Y-axis are truncated at 1000, thus removing the very high data points for RBCL (between 2176 and 3105). (**B**) Principal component analysis **(**PCA) of the 3 biological samples for each genotype, illustrating reproducibility between replicates and separation of the two genotypes (*fmtclpc1* and *clpc1*). **(C)** Relative protein investments in the five complexes of the photosynthetic electron transport chain (Photosystem II (PSII), Photosystem I (PSI), the cytochrome b6f complex (cytb6f), NDH complex (NDH) and ATP synthase (CF), as well as proteins of the Calvin-Benson cycle. The *fmtclpc1/clpc1* ratios are indicated for each complex.

Supplemental Table 1. FMT lines generated and/or used in this study

Mutant Name	Mutation site (genomic DNA, bp from start codon)	Mutation Effect	Note
fmt-3	Intron 19/27 (5799)	T-DNA insertion	SALK_046271 (El Zawily et al., 2014)
fmt-4	Exon 23/28 (6517)	T-DNA insertion	SALK_056717 (Larkin et al., 2016)
socc20-1	Intron 21/27, first base (6177)	Splice donor variant & intron variant	Splice defect (3150+1G>A)
socc20-4	Intron 22/27, last base (6514)	Splice acceptor variant & intron variant	Splice defect (3208-1G>A)
socc39-1	Intron 11/27, last base (3736)	Splice acceptor variant & intron variant	Splice defect (1876-1G/A)
socc43-1	Exon 10/28 (3201)	Missense variant	E534K (1600G>A)
socc43-1	Exon 21/28, last base (6176)	Splice region variant & synonymous variant	Splice defect 3150G>A

Exon and intron numbering is based on the reference gene model (total number of exons/introns indicated). Nucleotide positions are given as base pairs (bp) from the translational start codon in genomic DNA. Mutation effects were annotated using standard sequence ontology terms. T-DNA insertion lines (*fmt-3* and *fmt-4*) correspond to SALK collection alleles, with line identifiers and references provided in the "Note" column. For EMS-induced alleles, the "Note" column indicates the relevant cDNA position and amino acid or splice-site change. Together, these T-DNA and EMS-induced variants disrupt coding or splicing regions of *FMT*, supporting its role as the causal gene underlying the *socc* mutant phenotypes. All mutation sites were confirmed by DNA sequencing.

Supplemental Table 2. Primers used in this paper

	Primer 1 (5' --> 3')	Primer 2 (5'--> 3')
clpc1-1 genotyping (gene specific)	CTA GAA GAC CCA TGT CGA GTG TTA TAA C	GTC ACA ATT ACA TTG GAT CCG AGC ACC
clpc1-1 genotyping (gene and T-DNA)	CTA GAA GAC CCA TGT CGA GTG TTA TAA C	GCG TGG ACC GCT TGC TGC AAC T
fmt-3 genotyping (gene specific)	CTA TCA AAC TGC TGG GGG AAA AGC	CCA TCT CAA CAA GAT CTT TAG CCT C
fmt-3 genotyping (gene and T-DNA)	CTA TCA AAC TGC TGG GGG AAA AGC	GCG TGG ACC GCT TGC TGC AAC T
fmt-4 genotyping (gene specific)	GAT CTT CGG CCC GTA ATT AAG CAC	CCA TTT TGC CCA TGT CTT GAT ACA TC
fmt-4 genotyping (gene and T-DNA)	GAT CTT CGG CCC GTA ATT AAG CAC	GCG TGG ACC GCT TGC TGC AAC T
rec1-3 genotyping (gene specific)	GTA AGT TCA TCA TCG TGT TGC TGA G	CAT GGT CCA ACG AAT TCG CCT TTA TC
rec1-3 genotyping (gene and T-DNA)	GTA AGT TCA TCA TCG TGT TGC TGA G	GCG TGG ACC GCT TGC TGC AAC T
rec2-1 genotyping (gene specific)	CTG ATT TTC TTC TGA CAC TGG TCC TG	CTC CCA AGC CAG ACG CCT CTA TTT C
rec2-1 genotyping (gene and T-DNA)	CTG ATT TTC TTC TGA CAC TGG TCC TG	GCG TGG ACC GCT TGC TGC AAC T
rec3-1 genotyping (gene specific)	GAC TCC AAA TGC GTT CTC TAG GAC	CGT CAG ATG AAA TAC ACA GCA CAT G
rec3-1 genotyping (gene and T-DNA)	GAC TCC AAA TGC GTT CTC TAG GAC	TAG CAT CTG AAT TTC ATA ACC AAT CTC GAT ACA C
clpr2-1 genotyping (gene specific)	CTT CAT TGA GAT CGT GAG ATT GGT T	CTC AGA TTG GAG CAG CAA AAG CCC
clpr2-1 genotyping (gene and T-DNA)	CTT CAT TGA GAT CGT GAG ATT GGT T	GCG TGG ACC GCT TGC TGC AAC T
clpt1-2 genotyping (gene specific)	CAC TAG CAC AGT TGC TAA GTT CCT G	CCT ACC CAG CAT CCA TAT GAA GAC A
clpt1-2 genotyping (gene and T-DNA)	CAC TAG CAC AGT TGC TAA GTT CCT G	CCC ATT TGG ACG TGA ATG TAG ACA C
clpt2-1 genotyping (gene specific)	ATG GCG GCT CAC TCT TCT TGC AAC	GAT CCA GAG CAG AGT CAA GTG CTC TTT G
clpt2-1 genotyping (gene and T-DNA)	ATG GCG GCT CAC TCT TCT TGC AAC	TAG CAT CTG AAT TTC ATA ACC AAT CTC GAT ACA C
ppi1-1 genotyping (gene specific)	ATG GGG TCT CTC GTT CGT GAA TG	GAA CCA GCC CGG ATA GTT TTG AGG
ppi1-1 genotyping (gene and T-DNA)	ATG GGG TCT CTC GTT CGT GAA TG	ATA ACG CTG CGG ACA TCT AC
tic40-4 genotyping (gene specific)	GAT GTT CAT TGG GTT CTC TGA GC	GAG GAG ATG AGG AAC CCA GAA AC
tic40-4 genotyping (gene and T-DNA)	GAT GTT CAT TGG GTT CTC TGA GC	TAG CAT CTG AAT TTC ATA ACC AAT CTC GAT ACA C
gun1-101 genotyping (gene specific)	CTT TTC AGC GAT TCT GAA TGC	CAT GTT GCA TTT TGA CAG GTG
gun1-101 genotyping (gene and T-DNA)	CTT TTC AGC GAT TCT GAA TGC	TAG CAT CTG AAT TTC ATA ACC AAT CTC GAT ACA C
Genomic *FMT* cloning	ATC TCG GTC GGT G GGATCC GG CTA AAA G	CTT TGA GCA CCA TTT TCC TTC AAG ATC CTA CTG CGG CCG CTT TTT TGG CTT TTT GCT TCT TCT TAT CCA AAG ATG
Genomic *CLPC2* cloning	CTT CTG CAG AAT TCT TAC TAA GAT GTC AG	GTT GCG GCC GCC AAT ATT GGA ATA GGA TCT TCC ATG GCT TCT TCA G
CLPC1-sgRNA1	ATT GAT GTC CCT GAA ACT ATT GAA	AAA CTT CAA TAG TTT CAG GGA CAT
Cas9 genotyping	TCG TTT TCT CTG CCG TCT CT	ATG GTG GGG TAC TTC TCG TG
ACTINII semi RT-PCR	CAA ACG AGG GCT GGA ACA AGA CT	GCA ACT GGG ATG ATA TGG AAA AGA
CLPC1 semi RT-PCR	GTC ACA ATT ACA TTG GAT CCG AGC ACC	CTA GAA GAC CCA TGT CGA GTG TTA TAA C
FMT-1F1R semi RT-PCR	GAA GTC ATG GAA AAG AAA GCC TCT G	GTG CAA ACA CTC TGG ATC AGT TGG
FMT-2F2R semi RT-PCR	CTA TCA AAC TGC TGG GGG AAA AGC	CCA TCT CAA CAA GAT CTT TAG CCT C
FMT-3F3R semi RT-PCR	GAT CTT CGG CCC GTA ATT AAG CAC	CCA TTT TGC CCA TGT CTT GAT ACA TC
FMT-4F4R semi RT-PCR	CAC GAG ACT CTC TAA ATT GGA TGA AG	TTA TTT TTT GGC TTT TTG CTT CTT CTT ATC
PP2A RT-qPCR	GCG GTT GTG GAG AAC ATG ATA CG	GAA CCA AAC ACA ATT CGT TGC TG
SAND RT-qPCR	TTG ATC CAC TTG CAG ACA AGG C	TAC CCT TTG GCA CAC CTG ATT G
Clathrin RT-qPCR	CTG ACT GGC CCT GCT T	ATA CGC GCT GAG TTC CC
CLPC1 RT-qPCR	ATT GAG CTT CAG GTG ACC GA	TAG CAC CGT GAC GTT ACC TT
CLPC2 RT-qPCR	GCG GAG AAG ATG CTT TCA AGG	TTG GAA TAG GAT CTT CCA TGG CT
CLPD RT-qPCR	GAA CAA AGG GTC TGG GCT TG	CCT CGC TTG GCT CGT TAA TC
REC1 RT-qPCR	AGC TGA TGG AAC GGA ACC TT	GTG GGC TTA ACT CCT CAC TCT
REC2 RT-qPCR	TCT GAG GAG AAG GGA AG	CAC TTG CCT CCT TGT CGT TC
REC3 RT-qPCR	GGG CGG TTA TTG CAT CTG TT	TCT GTA GCC ACT GTA ATC TGA G
FMT RT-qPCR	CGT CCC TGT ATG CTC TGA GG	TGC AAC TTC CCT GTG CAT TG

Other Supplemental Materials (Excel file) for this manuscript include the following:

Supplemental Table 3. (Excel file) 99 Genes reported to be involved in mitochondrial or chloroplast dysfunction, stress response, retrograde signaling, biogenesis or proteostasis; these were collected from numerous published reviews.(Bittner *et al.*, 2022; He *et al.*, 2023; Hernandez-Verdeja, 2025; Wang *et al.*, 2018; Wang *et al.*, 2020) Differential RNA-seq expression for 48 of these genes is represented in the cladogram as depicted in Fig. 4B and included in Supplementary Data Set 1B.

Supplemental Data Set 1. (Excel file) RNA-seq datasets for Col-0*, fmt, clpc1, fmtclpc1* and *FMT/clpc1*. (A) RNA abundance (normalized read counts per replicate) of 21202 genes in Col-0, *fmt*, *clpc1*, *fmtclpc1* and *FMT/clpc1*. This includes plastid- and mitochondrial encoded genes and non-protein coding genes, but these genes are otherwise excluded from the analyses presented in this study. These data are deposited in GEO. **(B)** Nuclear protein-coding genes (4745 genes) that show at least one pairwise significance difference (adj P<0.01 and at least 2-fold difference) between two genotypes (total 10 pairwise comparisons). Predicted proteins are annotated for name, subcellular location (annotated and predicted) and function (MapMan bin system) based on information from TAIR and PPDB. Normalized average RNA abundance per genotype and their cluster membership (from the cladogram in Fig. 4B) are listed for all genes. RNA expression ratios for each of the 10 pairwise genotype comparisons are listed whenever the adj P value is <0.01.

Supplemental Data Set 2. (Excel file) MS-based comparative proteomics datasets of total extracted proteomes of aboveground seedlings of *clpc1-1* and *fmtclpc1-1*. (A) Identification and annotation of 2976 proteins by nanoLC-MS. **(B)** Quantification and significance analysis of 1529 identified proteins and protein groups with at least 12 adjSPC.